NASA Technical Paper 3596

Numerical Simulation of Jet Aerodynamics Using the Three-Dimensional Navier-Stokes Code PAB3D

S. Paul Pao
Langley Research Center • Hampton, Virginia

Khaled S. Abdol-Hamid
Analytical Services & Materials, Inc. • Hampton, Virginia

National Aeronautics and Space Administration
Langley Research Center • Hampton, Virginia 23681-0001

September 1996

Available electronically at the following URL address: http://techreports.larc.nasa.gov/ltrs/ltrs.html

Printed copies available from the following:

NASA Center for AeroSpace Information
800 Elkridge Landing Road
Linthicum Heights, MD 21090-2934
(301) 621-0390

National Technical Information Service (NTIS)
5285 Port Royal Road
Springfield, VA 22161-2171
(703) 487-4650

Contents

Abstract 1
Introduction 1
Symbols 2
Governing Equations 3
  Navier-Stokes Equations 3
  Jones-Launder Two-Equation Turbulence Model 3
Grid Adaption Strategy 4
Computational Methods 6
  Solver Algorithm 6
  The k-ε Turbulence Model 6
  Multiblock Structure and Boundary Conditions 7
  Adaptive Grid Algorithm in the PAB3D Code 7
Results and Discussion 7
  On-Design Circular Jet Plumes 8
  Off-Design Jets Containing Weak Shocks 10
  Off-Design Supersonic Jets Containing a Mach Disk 11
  Adaptive Grid Computations of Nonaxisymmetric Jets 12
Concluding Remarks 14
References 15
Figures 16

Abstract

This report presents a unified method for subsonic and supersonic jet analysis using the three-dimensional Navier-Stokes code PAB3D. The Navier-Stokes code was used to obtain solutions for axisymmetric jets with on-design operating conditions at Mach numbers ranging from 0.6 to 3.0, supersonic jets containing weak shocks and Mach disks, and supersonic jets with nonaxisymmetric nozzle exit geometries. This report discusses computational methods, code implementation, computed results, and comparisons with available experimental data. Very good agreement is shown between the numerical solutions and available experimental data over a wide range of operating conditions. The Navier-Stokes method using the standard Jones-Launder two-equation k-ε turbulence model can accurately predict jet flow, and such predictions are made without any modification to the published constants for the turbulence model.

Introduction

Knowledge of jet mixing aerodynamics is vital to several areas of commercial and military aircraft design, such as jet propulsion efficiency, propulsion integration, aeroacoustics, and jet interference with aircraft structure. Initial jet flow conditions are determined by nozzle exit pressure, temperature, Mach number, and nozzle geometry. Once the flow leaves the jet nozzle, the jet flow becomes a free shear layer. The action of turbulence dominates flow developments farther downstream. As such, jet flow properties are difficult to measure or predict analytically.

When Prandtl introduced his mixing length hypothesis for turbulent flows, a brief analysis of a fully mixed jet was given as an example. Early analyses of jet mixing behavior were based mainly on this mixing length hypothesis and one-dimensional momentum theory. (See refs. 1–4.) Mean flow properties derived from these analytical models compare well with experimental measurements of jets at low subsonic speeds. However, data from jet flow measurements in the high subsonic and supersonic speed ranges (ref. 5) indicate significant departure from the results obtained by using one-dimensional momentum theory.

Jet flow contains a rich combination of flow interactions and flow physics. These combinations include turbulent mixing and compressibility effects such as isentropic expansion and shock. Other factors may include chemical reactions or shear layer instability.

Subsonic jet flow features are relatively simple. The main variable in the flow is shear layer development along the streamwise direction. The static pressure value is almost constant with the ambient pressure. In the absence of a pressure gradient, no significant inviscid flow feature will appear in a subsonic jet. According to reported experimental measurements, all turbulent axisymmetric subsonic jets below Mach 0.6 are similar if the flow variables are normalized by jet density and nozzle exit velocity.

On the other hand, supersonic jet flow features can be very complex. Because of the supersonic nozzle exit Mach number, jet exit pressure can differ from ambient pressure. This pressure difference between the jet and the ambient fluid must be resolved locally either across an oblique shock, by a prominent streamline curvature at the jet boundary, or by a Mach disk inside the jet. In addition, shocks formed near the nozzle exit may reflect repeatedly at the sonic line in the shear layer. Although the convected turbulence interacts with shocks in the jet, the position of the reflected shock depends on the location of the sonic line in the turbulent shear layer. Such interdependence of flow interactions can become very complex.

Earlier jet flow analysis codes, with or without chemical interactions included, were formulated with simplified assumptions of the Navier-Stokes equations and the turbulence model to provide the best jet flow simulation within modest limits of computing resources available during this time. Analytical methods and simulation codes developed by this approach have been successfully applied to problems in air-breathing engine development, acoustics, and rocket propulsion. (See refs. 6–12.) However, there are some drawbacks to this approach. First, simplified assumptions are often difficult to justify. Second, application of the simplified formulations is limited to jet flow simulation. The formulations are difficult to integrate with computational codes for airframe aerodynamics when performing propulsion airframe integration analysis. It is preferable in such cases to perform the analysis with the three-dimensional Navier-Stokes equations without empirical assumptions for jet flow alone.

For general use of jet flow simulation, some basic requirements must be met. The Navier-Stokes code should be upwind biased to capture internal shocks and

other jet flow discontinuities. The code should also be fully three-dimensional in space because the relations between turbulent kinetic energy and Reynolds stresses are basically three-dimensional. The turbulence model should be capable of providing a time scale and a consistent description of the production and transport properties of turbulent kinetic energy. Therefore, a two-equation turbulence closure model is required.

Many upwind-biased three-dimensional Navier-Stokes codes are available that meet the jet flow simulation requirement. However, the availability of codes with a robust two-equation turbulence mode in this class is limited. In this report, the PAB3D code is used for all jet flow computations. The purpose of this report is to show the feasiblity of establishing a unified method for subsonic and supersonic jet analysis with a general purpose three-dimensional Navier-Stokes code.

The PAB3D code is developed to obtain numerical solutions to the Reynolds averaged Navier-Stokes equations in three-dimensional spatial domain. The main solver algorithm is the upwind Roe scheme, for which the numerical dissipation is small. The Jones-Launder (ref. 13) two-equation k-ε turbulence closure model is used to compute the turbulent stresses in the flow. This approach is chosen for jet flow analysis because it is consistent in tracking production and transport properties of turbulence kinetic energy and dissipation scale length in the shear flow. In the Jones-Launder k-ε turbulence model, several empirical constants are required. Only the published values for these constants are implemented in the PAB3D code. These values are fixed for all computational applications of the PAB3D code.

This report describes the mathematical formulation of governing equations, the turbulence model, and the adaptive grid generation algorithm, along with the numerical implementation of each. The adaptive grid generation algorithm is designed especially for nonaxisymmetric jet computations.

Several categories of jet flow computations are described separately in the section “Results and Discussion.” The first category describes axisymmetric jets operating at on-design exit conditions so that the jet exit pressure matches the ambient static pressure. Results are obtained for jet exit Mach numbers ranging from 0.6 to 3.0. Computed velocity and turbulence intensity distributions in the jet are compared with experimental data. The second category presents results for supersonic jets with internal weak shocks. The discussion includes computed results for jet exit pressures above and below the ambient static pressure to show characteristics of the shock-containing supersonic jets. Computed results are compared with available experimental data. The third category of computed cases is axisymmetric supersonic jets with embedded Mach disks. Flow conditions for these jets are the result of a supersonic jet nozzle operating at pressures far from nozzle design value. One particular case details a Mach 1.5 nozzle operating at a nozzle pressure ratio 3.15 times greater than the design value for this nozzle. The last category includes supersonic jets with nonaxisymmetric initial cross sections. Shear layer development of these jets is very different from a typical axisymmetric jet because of added geometrical degrees of freedom. The development of elliptic, rectangular, and square jets operating at the same exit pressure and Mach number is compared.

Symbols

a	local speed of sound
e	internal energy per unit mass
C_1, C_2, C_μ	constants in two-equation turbulence model
F, G, H	inviscid flux components in Navier-Stokes equations
F_v, G_v, H_v	viscous flux components in Navier-Stokes equations
$\hat{F}$, $\hat{G}$, $\hat{H}$	total flux vectors (inviscid plus viscous) in Navier-Stokes equations
f_1, f_2, f_n	monitoring function for grid adaptation
i, j, k	grid index in ξ-, η-, ζ-directions
J	Jacobian of coordinate transformation
k	turbulent kinetic energy
L_c	jet potential core length
l_1	shock cell length measured from nozzle exit to first shock intersection at jet centerline
M	Mach number
NPR	nozzle pressure ratio, $\frac{p_t}{p_o}$
n	distance in a direction normal to a solid wall
$\bar{P}$	production term for turbulent kinetic energy
p	pressure
p_e	jet exit static pressure
p_o	ambient static pressure
p_t	jet total pressure
$\hat{Q}$	conservative variable vector in Navier-Stokes equations
R	jet exit radius or area equivalent radius

S	source function in Navier-Stokes equations
T	temperature
t	time
U_e	jet exit velocity
U_c	jet centerline velocity
u, v, w	velocity components in x-, y-, and z-directions
u_i'	components of turbulence velocity fluctuation
u_{rms}	root-mean-square value of turbulence velocity fluctuation, $\sqrt{\overline{u_i' u_i'}}$
u_t	turbulence velocity fluctuation
W	shock cell length measured from nozzle lip to position of first shock reflection in shear layer
x, y, z	spatial coordinates
Γ	compressibility correction factor
δ_{ij}	Kronecker delta
ε	turbulent kinetic energy dissipation rate
μ	dynamic coefficient of viscosity
ν	kinematic coefficient of viscosity
ξ, η, ζ	generalized coordinate as function of x, y, and z
ρ	density
$\sigma_\varepsilon, \sigma_k$	constants in two-equation turbulence model
τ	shear and normal stress components

Subscripts and superscripts:

e	jet exit condition
k	turbulent kinetic energy
L	laminar quantities
o	free-stream condition
T	turbulence related quantities
v	viscous component of flux vectors
ε	turbulent energy dissipation

Governing Equations

The governing equations of the Reynolds averaged Navier-Stokes formulation include the conservation equations for mass, momentum, and energy and the equation of state for gas. In this study, the perfect gas law is chosen to represent the properties of air. For a turbulent flow, the Reynolds stresses can be represented by turbulence closure models for practical applications. Because one of the dominant factors governing jet dynamics is turbulent shear layer mixing, the turbulence closure model is essential for realistic jet flow simulation when using Navier-Stokes methods. The Jones-Launder (ref. 13) two-equation k-ε turbulence model is used in this study. The Navier-Stokes equations and the mathematical representation of the two-equation turbulence model are described briefly in separate subsections of this report.

For computation of nonaxisymmetric jet flows, a special requirement in grid generation arises. High grid density is required for regions occupied by the shear layer and the embedded shock so that high gradients of mean flow and turbulence quantities can be accurately represented in the numerical solution. However, the position of the shear layer and the shock positions of a nonaxisymmetric jet are not known in advance. This special requirement can be met by using an adaptive grid. The analytical basis for an adaptive grid is described in the report section "Grid Adaptation Strategy" following discussions of Navier-Stokes equations and the Jones-Launder k-ε turbulence model.

Navier-Stokes Equations

The mass, momentum, and energy conservation equations of the Reynolds averaged Navier-Stokes equations can be written in terms of generalized coordinates and in a conservative form as follows:

$$\frac{\partial \hat{Q}}{\partial t} + \frac{\partial \hat{F}}{\partial \xi} + \frac{\partial \hat{G}}{\partial \zeta} + \frac{\partial \hat{H}}{\partial \eta} = S \tag{1}$$

where t, ξ, η, and ζ are the independent variable for time and the general curvilinear coordinates in the grid domain, $\hat{Q}$ is the conservative flow variable vector (ρ, ρu, ρv, ρw, ρe) in generalized coordinates, $\hat{F}, \hat{G}, \hat{H}$ are the total generalized flux vectors including inviscid and viscous components, and the source term S is zero for the Navier-Stokes equations in this form. This equation is introduced here mainly to indicate the relationship between the basic Navier-Stokes equations and the two-equation turbulence model equations. Reference 14 presents details of the Navier-Stokes equations as applied in the PAB3D code. A simplified form of the Navier-Stokes equations which omits all the streamwise derivatives of the Reynolds stresses is used in the PAB3D code. Omission of these terms is done for computational economy and does not introduce significant computation error. The remaining cross stream derivatives are numerically implemented at several levels in PAB3D. The thin layer Navier-Stokes approximation is one option for the user. This study uses the option of uncoupled Reynolds stress derivatives in two directions.

Jones-Launder Two-Equation Turbulence Model

The Jones-Launder formulation for the two-equation turbulence model uses the turbulent kinetic energy k and the dissipation rate ε as the principal variables. This study uses the expanded three-dimensional form (ref. 15) of the original Jones-Launder model. This modified formulation is fully three-dimensional, and the governing equations are written in a conservative form as generalized coordinates. The governing equations can be cast in the same form as the Navier-Stokes equations, where

$$\hat{Q} = \begin{Bmatrix} \rho\varepsilon \\ \rho k \end{Bmatrix} \qquad F = \begin{Bmatrix} \rho u\varepsilon \\ \rho u k \end{Bmatrix} \qquad G = \begin{Bmatrix} \rho v\varepsilon \\ \rho v k \end{Bmatrix} \qquad H = \begin{Bmatrix} \rho w\varepsilon \\ \rho w k \end{Bmatrix}$$

$$F_v = \begin{Bmatrix} \mu_\varepsilon \dfrac{\partial\varepsilon}{\partial x} \\ \mu_k \dfrac{\partial k}{\partial x} \end{Bmatrix} \qquad G_v = \begin{Bmatrix} \mu_\varepsilon \dfrac{\partial\varepsilon}{\partial y} \\ \mu_k \dfrac{\partial k}{\partial y} \end{Bmatrix} \qquad H_v = \begin{Bmatrix} \mu_\varepsilon \dfrac{\partial\varepsilon}{\partial z} \\ \mu_k \dfrac{\partial k}{\partial z} \end{Bmatrix}$$

$$\bar{P} = \tau_{xx}^T \frac{\partial u}{\partial x} + \tau_{yy}^T \frac{\partial v}{\partial y} + \tau_{zz}^T \frac{\partial w}{\partial z} + \tau_{xy}^T \left(\frac{\partial u}{\partial y} + \frac{\partial v}{\partial x}\right) + \tau_{yz}^T \left(\frac{\partial v}{\partial z} + \frac{\partial w}{\partial y}\right) + \tau_{zx}^T \left(\frac{\partial w}{\partial x} + \frac{\partial u}{\partial z}\right)$$

$$S = \begin{Bmatrix} S_\varepsilon \\ S_k \end{Bmatrix}$$

$$S_\varepsilon = C_1 \bar{P}\frac{\varepsilon}{k} - C_2 \rho \frac{\varepsilon}{k}\left[\varepsilon - 2\nu\left(\frac{\partial\sqrt{k}}{\partial n}\right)^2\right] + L_\varepsilon$$

$$S_k = \bar{P} - \rho(1+\Gamma)\varepsilon + L_k$$

Here, $\bar{P}$ is the full three-dimensional production term defined as

$$\bar{P} = \tau_{xx}^T \frac{\partial u}{\partial x} + \tau_{yy}^T \frac{\partial v}{\partial y} + \tau_{zz}^T \frac{\partial w}{\partial z} + \tau_{xy}^T \left(\frac{\partial u}{\partial y} + \frac{\partial v}{\partial x}\right) + \tau_{yz}^T \left(\frac{\partial v}{\partial z} + \frac{\partial w}{\partial y}\right) + \tau_{zx}^T \left(\frac{\partial w}{\partial x} + \frac{\partial u}{\partial z}\right)$$

or is expanded to

$$\bar{P} = \mu^T \left\{ \left(\frac{\partial u}{\partial y} + \frac{\partial v}{\partial x}\right)^2 + \left(\frac{\partial v}{\partial z} + \frac{\partial w}{\partial y}\right)^2 + \left(\frac{\partial w}{\partial x} + \frac{\partial u}{\partial z}\right)^2 + 2\left[\left(\frac{\partial u}{\partial x}\right)^2 + \left(\frac{\partial v}{\partial y}\right)^2 + \left(\frac{\partial w}{\partial z}\right)^2\right] - \frac{2}{3}\left[\frac{\partial u}{\partial x} + \frac{\partial v}{\partial y} + \frac{\partial w}{\partial z}\right]^2 \right\} - \frac{2}{3}\rho k \left(\frac{\partial u}{\partial x} + \frac{\partial v}{\partial y} + \frac{\partial w}{\partial z}\right)$$

where

$$\mu^T = C_\mu \rho \frac{k^2}{\varepsilon} \qquad \mu_\varepsilon = \mu^L + \frac{\mu^T}{\sigma_\varepsilon} \qquad \mu_k = \mu^L + \frac{\mu^T}{\sigma_k}$$

$$C_\mu = 0.09$$

$$C_1 = 1.44 \qquad C_2 = 1.92 \qquad \sigma_\varepsilon = 1.3 \qquad \sigma_k = 1.0$$

$$\tau_{ij}^T = \mu^T \left[\left(\frac{\partial u_i}{\partial x_j} + \frac{\partial u_j}{\partial x_i}\right) - \frac{2}{3}\frac{\partial u_k}{\partial x_k}\delta_{ij}\right] - \frac{2}{3}\rho k \delta_{ij}$$

In the definitions of S_ε and S_k, the terms L_ε and L_k are near-wall effects which are not important to free jet calculations, and $\partial/\partial n$ denotes derivatives in a direction normal to the solid wall boundary. However, these terms are included in the PAB3D code. The function Γ is the compressibility correction function. Several corrections have been developed by different authors. Among the widely used compressibility correction functions Γ are those proposed by Sarkar et al. (ref. 16) and by Wilcox (ref. 17).

Sarkar model (ref. 16):

$$\Gamma = M_T^2 \tag{2}$$

Wilcox model (ref. 17):

$$\Gamma = (M_T^2 - M_{T,o}^2) H(M_T - M_{T,o}) \tag{3}$$

where H is the Heaviside function, $M_T = \sqrt{k/\rho}/a$ is the local turbulence Mach number, a is the local speed of sound, and $M_{T,o}$ is a cutoff turbulence Mach number. The commonly accepted value $M_{T,o} = 0.25$ is used in the PAB3D code. The compressibility correction factor is required when the local flow Mach number is greater than 1.0. In the Sarkar model, the compressibility correction is activated everywhere in the flow field when applied for a given computation. The Wilcox model is a modification of the Sarkar model so that Γ is nonzero only for values of M_T greater than $M_{T,o}$. This condition implies that compressibility correction is activated for local flow Mach numbers near or greater than 1, with no correction otherwise.

Grid Adaption Strategy

For an accurate representation of the flow field, sufficient grid density must be provided in the mixing region. Unlike an axisymmetric jet, the nonaxisymmetric jet is not self-similar and can evolve in dramatically different fashion in different sectors of the jet cross section. Because the position of the shear layer is not known in advance, a large number of predetermined grid points

are required to provide high density coverage of the three-dimensional space if a fixed grid is used for the computations. An alternative is to provide high grid density in the appropriate locations by using an adaptive grid strategy.

For jet plume analysis, high grid density is required in high velocity gradient regions in the shear layer and in high pressure gradient regions near shock fronts. The number of grid points in each direction of a structured grid is fixed. Local grid density can be varied by redistributing the available grid points in the computational domain to match selected flow characteristics such as pressure and velocity gradients. Various methods can be used to redistribute grid density according to given multiple functional requirements. In this study, the equidistribution principle and the alternate direction grid adaption method published by Eiseman et al. (refs. 15, 18, and 19) are chosen as the basis for adaptive grid implementation in the PAB3D code.

In the equidistribution approach, a monitoring function which governs grid density over the computation domain is defined. The monitoring function can be geometrically represented as a hypersurface in a space with dimensions that are one higher than the spatial dimensions of the computational domain. The process of grid adaption begins by constructing a uniform mesh over the monitoring surface. For a one-dimensional case, the monitoring surface is a curve over the linear spatial domain. Equidistribution is simply a uniform distribution of points at equal arc distances on the entire length of the monitoring curve. When this distribution of points is projected back to the one-dimensional baseline in the physical domain as adapted grid points, the grid density is proportional to the gradient of the monitoring function. For a two-dimensional grid domain, the monitoring surface is a curved surface in three dimensions over the two-dimensional physical space. The equidistribution process involves constructing a mesh system over the curved monitoring surface so that all the grid cells enclose approximately equal surface areas. Once the equidistribution construction is complete, the mesh pattern on the monitoring surface is projected onto the original physical domain. Similar to the one-dimensional case, high grid densities are again obtained in regions where the monitoring function has high gradients.

If the monitoring surface is assumed to represent mountains and valleys in a landscape, the previously mentioned process is similar to making a contour map of this landscape. Steep slopes in the landscape are naturally represented by tightly packed contour lines on the map, which is a horizontal projection of the original three-dimensional surface. Visualization of the monitoring surface can be difficult for a three-dimensional spatial domain. However, the algebra and the geometry for the adaption process remain unchanged. In addition to equidistribution of arc lengths or areas on the hypersurface, normal curvature of the monitoring surface can also be used as a weighting function to provide additional mesh density control.

The alternative direction adaption proposed by Eiseman simplifies the equidistribution procedure by performing arc length equidistribution on the monitoring surface along each family of coordinate lines. If cell skewness remains within reasonable limits, equidistribution of all sides of the grid cells will also distribute the cell area or volume into approximately equal sizes. However, orthogonality is not enforced in this procedure. The degree of grid concentration for given values of the gradients of a monitoring function is controlled by a proportional constant. Since orthogonality is not enforced in the alternate direction equidistribution procedure, excessive cell skewness and cell collapse can occur if the proportional constant is given too high a value.

For grid adaption to more than one flow quantity, multiple monitoring functions can be used. A simple approach is to combine all monitoring functions as a single weighted sum. The approach of Eisman and Brockelie (ref. 20) treats each monitoring function as an additional geometrical dimension (which is orthogonal to all previous dimensions). In this approach, grid features represented in each monitoring function remain distinct. The differential arc length element can be given as

$$ds_1 = 1 + w(s_0)\sqrt{1 + |\mathrm{grad}(f_1)|^2 + |\mathrm{grad}(f_2)|^2 + \ldots}\; ds_0 \quad (4)$$

where ds_0 is the arc length in the physical or grid domain, ds_1 is the arc length on the monitoring surface, grad denotes a component of the gradient in the tangential direction of the coordinate curves, and $w(s_0)$ is an optional weighting function which is proportional to the curvature of the monitoring surface.

A modified approach called the sequential adaption method is used in this paper. Assuming there are N monitoring functions, the monitoring functions are applied sequentially. After each step of adaption, the mesh on the previous monitoring surface is treated as a "stretched" uniform mesh to support the next monitoring function. The arc length increments on each of the monitoring surfaces can be written as

$$ds_n = 1 + w_n(s_{n-1})\sqrt{1 + |\mathrm{grad}(f_n)|^2}\; ds_{n-1} \quad (n = 1, 2, \ldots, N) \quad (5)$$

Once the adaption process is completed over the last monitoring function, the mesh coordinates are projected sequentially back to all previous base surfaces. The

last one is the physical space where an adapted grid is established.

Where the curvature weighting functions $w_1, \ldots, w_n$ are zero, the sequential adaption method and the vector monitoring function method are mathematically the same. Only their geometrical interpretation and computational implementation are different.

Computational Methods

The simplified Reynolds averaged Navier-Stokes equations and the Jones-Launder k-ε turbulence model are implemented in the PAB3D code for general fluid dynamics analysis in three-dimensional space. Distinctive features of this code include provisions to accept a multiblock grid with patched interface, compact memory requirement, and solver options. In particular, a space-marching solver with adaptive grid capability is available for jet flow computation when flow conditions meet the space-marching scheme criterion. For such cases, the space-marching solution accuracy is indistinguishable from accuracy obtained by using the time-marching solver algorithm. The space-marching procedure can complete a converged solution in approximately one-twentieth the computer time required by the time-marching solver to obtain a solution for the same flow conditions.

Solver Algorithm

Three numerical schemes have been implemented in the PAB3D code as solvers for the Navier-Stokes equations: the Van Leer flux-vector splitting scheme, the Roe flux-difference splitting scheme, and a space-marching scheme that is a modified version of the basic Roe scheme. These schemes are implicit, upwind, and constructed by using the finite volume approach. Only the inviscid portion of the flux vectors $\hat{F}$, $\hat{G}$, and $\hat{H}$ is subjected to the splitting and upwind procedures. The diffusion terms of the Navier-Stokes equations are centrally differenced. Reference 14 details mathematical description of these schemes.

The flux-vector scheme and the flux-difference splitting scheme are used in all three computational directions. An updated solution at each iteration is obtained by using an implicit procedure in the mesh η,ζ-planes at constant values of ξ and a relaxation procedure in the ξ-direction consisting of a forward and a backward sweep. This particular implementation strategy has an advantage for computational efficiency. Since the metrics for the implicit procedure are required for only up to three planes, the metric constants are recomputed one plane at a time at the advancing front of the prevalent sweep direction instead of being stored for the entire grid domain. Moderate or large mesh sizes require an average of only 22 words of memory for each gird point. This highly efficient use of computer memory is obtained at a modest cost of approximately a 3-percent increase in computer time per iteration. The overall computer time requirement per iteration per grid point is similar to other codes of this type.

For time-marching solutions using the Van Leer or the Roe scheme, each iteration count consists of either a forward or a backward sweep in the ξ-direction with one step of implicit update of the solution in each of the cross planes. The inviscid terms in the Navier-Stokes equations in the Roe scheme are cast in the form of an approximate Riemann problem. The interface flux in the streamwise direction is determined by separate terms, depending on the quantities on the left (upstream) and the right (downstream) sides of the interface. For a fully supersonic flow, the information can travel only in the flow direction. Such information is carried by the terms representing upstream dependence. The terms which carry the downstream dependence can be ignored without introducing significant flow solution error. This state of information transfer in the Roe scheme solver is true for a broad category of subsonic and supersonic jet flows where the streamwise pressure gradient is small. By ignoring the downstream dependence terms in the Roe scheme, the solver becomes the space-marching scheme. Under this modified scheme, a solution is obtained plane by plane from upstream to downstream by carrying out a sufficient number of implicit iterations in each plane until the convergence criterion is met. A solution for the entire computational domain is established in a single forward sweep.

The k-ε Turbulence Model

The governing equations of the Jones-Launder formulation of the k-ε turbulence model are written as a pair of coupled transport equations in conservative form. In principle, this pair can be implemented together with the Navier-Stokes equations as either a set of seven coupled equations or a separate pair uncoupled from the Navier-Stokes equations. The fully coupled approach would cause serious problems such as a significant increase in computational effort and working space in the computer memory and numerical stiffness of the coupled set of seven equations. In the PAB3D code, solutions of the k and ε equations are decoupled from the Navier-Stokes equations and from each other. Time step differences remain in this uncoupled system of flow and turbulence equations. However, the problem is circumvented by solving these k and ε equations with a CFL (Courant, Fredricks, and Levy) number that is smaller by at least a factor of 2. The potential difference in timewise development of the flow variables and turbulence variables

has not led to any noticeable effect in either the overall convergence rate or the quality of the solutions.

Multiblock Structure and Boundary Conditions

The PAB3D code is designed to handle complex configurations by using several types of multizone, multiblock grid topologies. A restricted option, which is suitable for jet plume calculation with the space-marching schemes, calls for streamwise division of the computational domain into zones in the ξ-direction. The grid space in each zone can further be divided into blocks in the η- and ζ-directions. Otherwise, the code supports a general multiblock scheme where the computational domain can be divided into any collection of blocks. Number of blocks, block size, and parametric orientation are not restricted. The concept of zones is not relevant in this general scheme. General patched block interface communication is allowed. The only restriction for this general multiblock connectivity scheme is that the connected block interfaces are contiguous. A grid partition feature is available in the PAB3D code for the convenience of turbulence modeling. If different viscous stress models are employed within a block, the ξ-direction of the block can be partitioned by choosing a starting index for each viscous stress model.

The boundary conditions often used for jet computations include inflow, outflow, free stream, solid walls, and geometrical symmetry. Three types of inflow boundary conditions are provided: Riemannian characteristics, fixed total temperature and total pressure, and a completely fixed set of five flow parameters. Two outflow boundary conditions are needed: constant pressure for subsonic flows and extrapolation for supersonic flows. The Riemannian characteristics boundary condition is used at free stream boundaries. On a solid boundary, either a no-slip or an inviscid-slip boundary condition can be specified. Finally, the symmetry boundary conditions include mirror imaging across a plane in any orientation and polar symmetry around an axis in the streamwise direction.

In addition, a universal high-order symmetry boundary condition for Navier-Stokes code applications is developed in the course of this jet plume study. This universal symmetry boundary condition provides a simple method for the user to specify a symmetry boundary condition at a grid plane not aligned to a surface with a constant physical coordinate value. Reference 14 details this boundary condition.

Adaptive Grid Algorithm in the PAB3D Code

For nonaxisymmetric jet calculations in this report, one quarter of the jet cross section is represented in the grid domain. Hence, flow symmetry across both the horizontal and the vertical axis is assumed. In each plane, the grid is divided into two parts: a high density grid in the near field of the jet flow and a low density grid for the far field. Only the high density grid near the jet flow is adapted to the flow solution. A Cartesian topology is chosen for the initial unadapted high density grid. Grid adaption proceeds from plane to plane in the streamwise direction. Two monitoring functions are used for adapting the grid to the velocity and pressure gradients of the flow solution. The monitoring functions are normalized so that one constant is used for each function to control the intensity of adaption. (See ref. 21.) A single grid was used in reference 21 to cover both the near field and the far field. A third monitoring function was employed to redistribute a uniform Cartesian grid to form a dense grid zone in the near field and a sparse grid distribution in the far field.

The adaptive grid procedure is coupled to the space-marching solver in PAB3D. Grid indices i, j, and k are assigned to the ξ, η, and ζ coordinates of the generalized coordinates. In the space-marching algorithm, a numerically converged solution is computed at each j, k-plane through multiple iterations. This solution is then coupled to the next plane downstream, and the computational process is repeated.

For jet flow computations considered in this report, initial conditions for the first plane representing the flow condition at the nozzle exit are prescribed according to known nozzle operating conditions. The initial grid at the first plane is generated externally according to the initial flow conditions by using the same grid adaption procedure as the one implemented in the PAB3D code. Once the solution process is started, grid adaptions for subsequent grid planes are computed within the code. A grid is created for the $(i + 1)$-plane by adapting the grid to the numerically converged solution in the i-plane. The adaptive grid procedure is implemented as efficiently as possible to match the high efficiency of the space-marching solver. The computational efficiency of this multiple function grid adaption procedure is analyzed during this study. The time taken for grid adaption is approximately 4 percent of the total time required for the flow solver. Only 1 cycle of adaption is used for each plane. The flow solution at each plane normally takes approximately 20 to 30 iterations before nominal convergence criterion is met.

Results and Discussion

Results of jet flow computations are presented in several groups: jets operating at on-design conditions, supersonic jets containing weak shocks, supersonic jets containing strong shocks, and nonaxisymmetric supersonic jets. For these groups of computation, the initial

flow condition for the jet is specified at the inflow boundary of the computational grid. The internal flow upstream of the jet nozzle is not modeled. Figure 1 shows a sketch of the jet flow configuration and a typical computational grid for on-design axisymmetrical jets.

On-design operation of a jet is defined as the condition for which the jet exit static pressure is identical to the ambient static pressure. For a subsonic jet, the exit static pressure is naturally adjusted to the ambient static pressure. A supersonic jet flow is established by using a convergent-divergent nozzle designed for a fixed Mach number. The on-design nozzle pressure ratio (NPR), defined as p_t/p_o, is a fixed value for each given Mach number. For jets operating at on-design NPR, pressure gradients are very small in the entire flow domain. Shocks in the flow domain are typically weak or absent in on-design supersonic jets. The principal driving mechanism for on-design jet plume development is turbulent mixing in the jet shear layer. This report computes on-design jet flows by using the space-marching scheme in PAB3D.

At off-design operating conditions, the initial jet flow condition is either overexpanded or underexpanded. Shock waves will appear in the jet flow. For a given nozzle geometry, the exit jet Mach number is fixed regardless of NPR (assuming that the NPR is high enough to fully establish supersonic flow at the nozzle exit). At NPR values sufficiently close to the design point, only weak shocks are present in the jet flow and jet flow development can be computed using the space-marching solver in PAB3D.

Once strong shocks in the form of Mach disks appear in the jet plume, the flow downstream of the shock becomes subsonic. Furthermore, high static pressure immediately downstream of the shock leads to rapid acceleration and expansion of the subsonic flow. Hence, a strong pressure gradient exists. The time-marching solvers in the PAB3D code must then be used because conditions permitting the use of the space-marching scheme are violated in this region. However, the space-marching method alone cannot detect the occurrence of a Mach disk. The decision to use either the space-marching or time-marching options in the PAB3D code for a particular case must be guided by tabulated experimental data or by theoretical estimates. Reference 5 gives an excellent reference for Mach disk formation in axisymmetric jet plumes.

Jet exhaust nozzles of practical interest in propulsion systems may have a nonaxisymmetric exit cross section. The dynamic characteristics of nonaxisymmetric jets are significantly more complex than those for axisymmetric jets because of the added degrees of freedom in jet flow geometry. The adaptive grid option in the PAB3D code is used to provide appropriate grid density distribution for the shear layer and shock regions in the jet flow. The following subsections give detailed discussions of results in each group of jet flow computations.

On-Design Circular Jet Plumes

Flow solutions for on-design circular jets within jet exit Mach numbers ranging from 0.6 to 3.0 are computed using the space-marching method in the PAB3D code. In this series of jet flow simulations, the initial flow condition for the jet plume is specified at the inflow boundary of the computational domain. A small velocity component in the ambient air parallel to the jet flow direction is required in the PAB3D code for maintaining numerical stability of the space-marching scheme. A freestream Mach number of 0.001 is sufficient in fulfilling this numerical requirement.

The on-design jet grid is constructed as a single layer wedge which covers a sector of 2.5° in the circumferential direction. Figure 1 shows general layout of this grid. There are 400 uniformly sized grid cells in the streamwise direction covering a distance of $x/R = 40$ and 48 grid cells in the transverse direction covering a radial distance of $y/R = 8$. At the inflow station of the jet, the jet plume is defined by 18 grid cells, and the remaining 30 grid cells cover the distance from $y/R = 1.0$ to 8.0. The initial shear layer region near the nozzle exit plane is covered by 24 grid cells centered above and below the nozzle lip. High grid density is provided in the shear layer to capture the turbulent mixing process. As the jet flow spreads downstream, approximately 30 grid cells are located within the jet flow. For computational convenience, the grid domain is divided into four blocks in the streamwise direction. The grid domain can easily be extended in the streamwise direction by adding more blocks.

General features of jet flow computation using the PAB3D code with the two-equation k-ε turbulence closure model are illustrated by the solutions of a typical subsonic jet at $M = 0.6$. Compressibility correction for the k-ε turbulence model is not needed in this computation. Figure 2 shows the computed centerline velocity profile for the $M = 0.6$ jet. The centerline velocity maintains its exit value for a distance up to approximately $x/R = 12$ and decreases farther downstream as a result of turbulence mixing. The classical relation of velocity decay is given by

$$\frac{u_c(x)}{U_e} = \frac{L_c}{x} \tag{6}$$

where L_c is the intercept of the x^{-1} decay curve and horizontal line $u_c(x)/U_e = 1.0$ (referred to as the potential

core length in jet flow literature). Figure 2 shows both the computed centerline velocity profile and the classical velocity decay as indicated by equation (6). Good agreement is shown between the PAB3D solution and the result obtained with equation (6).

Figure 2 also shows the computed centerline velocity profiles for a Mach 2.0 jet operating on-design using the Jones-Launder k-ε turbulence model with three different methods of compressibility corrections. The compressibility correction factor in the k-ε turbulence model has a strong influence on jet flow development. Turbulence mixing is strongest in the jet flow when no compressibility correction is applied. For this case, the potential core length is $L_c/R = 17.2$. The action of turbulence mixing in the jet is weaker when compressibility corrections are applied. The value of L_c/R is 22.6 and 25.2 for the Sarkar and the Wilcox methods, respectively. The velocity decay downstream of the end of the potential core is also computed according to equation (6) and the value of L_c/R for each case. The results are shown in figure 2.

Good agreement is observed between the PAB3D solutions using the Sarkar and the Wilcox corrections and their corresponding results using equation (6) for u_c/U_e greater than 0.7. For u_c/U_e less than 0.7, the PAB3D solution begins to deviate from the classical $1/x$ decay rate. For the solution without compressibility correction, the decay rate starts to deviate from the $1/x$ decay at approximately $u_c/U_e = 0.8$. Without compressibility correction in the k-ε turbulence model, the predicted turbulence level is too high for the Mach 2.0 supersonic jet solution. This steep velocity decay is an indication of excess mixing in the jet shear layer.

Figure 3 shows the downstream evolution of the $M = 0.6$ jet velocity cross section. At $x/R = 0$, the initial velocity profile across the entire width of the jet nozzle exit has a prescribed constant value of U_e. The cross section at $x/R = 5$ (fig. 3) shows the initial development of a thin shear layer, and the width of the potential core is narrower than its width at the jet exit. The cross section at $x/R = 15$ is located just downstream of the end of the potential core. The velocity profile at $x/R = 15$ has not yet attained a Gaussian distribution. However, the Gaussian velocity distribution has been established at $x/R = 25$. Figure 4 shows the turbulence intensity distributions at the corresponding x/R stations. The peaks of the turbulence intensity distributions at $x/R = 5$ and 15 are located in the middle of the shear layer where the velocity gradient is the highest. Although the centerline turbulence level at $x/R = 25$ is significantly higher, the peak turbulence intensity remains off center, and the turbulence intensity distribution across the jet is not Gaussian. According to measured data by Wygnanski and Fiedler (ref. 22), self similarity of the turbulence intensity is usually established at x/R values between 50 and 70.

Figure 5 shows computed centerline velocity profiles for a $M = 2.22$ jet and the experimental data measured by Eggers. (See ref. 23.) Like the centerline velocity profiles for a Mach 2.0 jet shown in figure 2, the solutions obtained by using different compressibility corrections are different. With no compressibility correction, the potential core length is underpredicted. The location of the end of the potential core appears to agree with the centerline velocity profile predicted using the Wilcox model. However, centerline velocity computed by using equation (6) and the potential core length of the Sarkar solution $L_c/R = 27.15$ agrees very well with the data obtained farther downstream. (See ref. 23.) The agreement between computational and measured data is much better when compressibility corrections are applied, although a small difference exists between the Sarkar model and the Wilcox solutions. Figure 6 shows the corresponding results of velocity distributions in the jet cross section at $x/R = 25$. The importance of compressibility correction for supersonic jets is further illustrated here, as the compressibility-corrected computations come very close to the measured data, whereas the uncorrected computation underpredicts the centerline velocity by nearly 40 percent.

A group of on-design jet plumes with exit Mach numbers ranging from 0.6 to 3.0 is computed to illustrate the trend of turbulent mixing as a function of Mach number. Figure 7 shows typical turbulence intensity distributions u_t/U_e in the longitudinal plane of symmetry of the jet at three different Mach numbers: 0.8, 1.2, and 1.6. The contours in figure 7 show that turbulence is absent in the potential core region. Intense levels of turbulence start to develop at the lip of the jet nozzle exit. The position of the maximum turbulence intensity in the initial zone of the shear layer occurs near the lip line of the jet. As the shear layer evolves farther downstream, the position of maximum turbulence intensity migrates towards the jet centerline. This general pattern remains the same for all on-design circular jets computed within the Mach number range from 0.6 to 3.0. The length of the potential core and the value of maximum turbulence intensity vary as a function of Mach number. Figure 8 summarizes the computed turbulence intensity distributions along the jet centerline as a function of Mach number. The Wilcox compressibility correction is used for these computations because the definition of the Wilcox correction provides a consistent blending of compressibility correction for subsonic and supersonic flow regions.

The potential core length is usually defined as the distance from the jet exit to the beginning of centerline velocity decay. An important equation for potential core

length as a function of jet Mach number is given by Lau, Morris, and Fisher in reference 24 as:

$$\frac{L_c}{R} = 8.4 + 2.2M^2 \tag{7}$$

Core length is obtained by an empirical curve fit to a large collection of measured values for potential core length in subsonic and supersonic jets.

Figure 9 shows the potential core lengths computed with the standard Jones-Launder two-equation k-ε turbulence model with the Sarkar and the Wilcox compressibility corrections. The core length is defined as the point where the value of the centerline jet velocity has dropped to 0.99 times the jet exit velocity. The potential core length derived with the Wilcox compressibility correction is higher than the value computed in equation (7) for the entire Mach number range. Values obtained by using the Sarkar compressibility correction are higher than the Wilcox results. However, the trends of core length variation as a function of Mach number are similar in all three sets of results. An alternate value of the potential core lengths can be obtained from the computed jet flow solution when the end of potential core in the jet flow is defined as the point where turbulence intensity level exceeds a threshold of $u_{rms} = 0.01$ along the jet centerline. The core lengths obtained by the turbulence intensity definition (also shown in fig. 9) agree very well with the values obtained with the velocity decay criterion.

The difference between the computed and the empirical curve fit formula based on measured values originates from several sources. In the work by Lau, Morris, and Fisher, the experimental database contains measured potential core length values for jets operating at different temperatures. Equation (7) is a curve fit for isothermal jets where the jet static temperature is the same as the ambient temperature, whereas the jet total temperature is higher than the ambient total temperature. Many data points for cold jets, where the jet total temperature is the same as the ambient air temperature and therefore the jet static temperature is colder than the ambient temperature, are above the curve fit of equation (7). In this report, the jet flows are computed as cold jets.

A second source of discrepancy may come from modeling boundary conditions in the computations. For jet flows in the laboratory, the boundary layer within the jet nozzle has a finite thickness at the nozzle exit. The initial turbulence level and the thickness of the nozzle boundary layer give the jet mixing layer an earlier start in its development. Therefore, the computed core length will be shorter if the initial boundary layer at the jet nozzle exit is included in the computations. In addition to these circumstances, grid density and accuracy of turbulence modeling are important factors to be considered for further refinements of the computational method for jet flow predictions.

It is significant that the mean flow and turbulence levels of on-design circular jet plumes are predicted over such a wide range of Mach numbers by using the standard Jones-Launder k-ε turbulence model and the Wilcox compressibility correction without changing the published constants for the turbulence model. In a broader context, the modeling of jet plumes is often required in propulsion and airframe integration. A consistent computational analysis for such jet plume modeling using the Navier-Stokes method should not permit ad hoc changes to the turbulence model. The results of this parametric investigation indicate that ad hoc modifications to the standard Jones-Launder turbulence model are not needed for jet flow analysis.

Off-Design Jets Containing Weak Shocks

This section shows the flow properties of a Mach 2 jet containing weak shocks using solutions obtained within a limited range of nozzle pressure ratios. The space-marching solver procedure in the PAB3D code is used to compute these jet flows. At Mach 2, the jet flow is free from Mach disk formation for values of NPR between 4.6 and 13.8, which correspond to a ratio of jet exit to ambient pressure p_e/p_o between 0.6 and 1.8. Figure 10 shows a density contour for a typical underexpanded jet. At the jet exit, a curved shock near the lip line of the jet nozzle is formed to resolve the pressure difference between the ambient flow and the flow inside the jet. An internal weak shock system which reflects repeatedly between the shear layer and the jet centerline also exists in the jet.

Figure 11 shows the computed pressure distribution along the jet axis for $p_e/p_o = 0.8$, 1.2, 1.4, 1.6, and 1.8. Only one overexpanded case is included in this collection ($p_e/p_o = 0.8$). The pressure distribution of the overexpanded jet is characterized by a sharp shock front and pressure peak close to the jet exit. This feature is not found in underexpanded jets. Beginning with the second peak, the features of overexpanded jet pressure oscillations on the jet centerline follow the same trend as the patterns shown for underexpanded jets. For the underexpanded jets, the cycle of pressure oscillation begins with a smooth expansion. The flow is then recompressed towards the first pressure peak in two stages. The pressure rises sharply about halfway then recompresses gradually the rest of the way. Although not shown in the figure, expansion and recompression processes are smooth for subsequent periods of oscillation. Reference 25 gives further discussion of the centerline pressure distributions of off-design jet flows at Mach 2.

Extensive flow visualization measurements of supersonic jets at off-design conditions were obtained by Love et al. (See ref. 5.) Shock formation in the jet flow is characterized by two lengths: l_1, the distance from the jet exit to the first shock intersection with the jet centerline; and W, the distance from the jet exit to the first shock intersection with the sonic line in the shear layer. Figure 10 shows definitions of these lengths. Figure 12 shows the computed values and measured values of l_1 and W (ref. 5) for several overexpanded and underexpanded values of NPR. Excellent agreement is demonstrated by the results in figure 12.

Figure 13 details computed centerline pressure distributions and experimental data for a Mach 2.0 jet at $p_e/p_o = 1.445$ (NPR = 11.3). Three solutions are obtained by using the basic k-ε turbulence model with no compressibility correction, the Sarkar correction, and the Wilcox correction. The solution without compressibility correction shows that the amplitude of pressure oscillations diminishes rapidly downstream and predicted wavelength is much shorter than the experimental data in the downstream region of the jet. The solutions obtained with a compressibility-corrected k-ε turbulence model show excellent agreement with measured data. Differences between the Sarkar and Wilcox corrections are small. The amplitudes of the computed solutions closely follow the test data, but their phase relations with respect to the measured data are somewhat different. At $x/R = 40$, the Wilcox solution leads the measured data by approximately one sixth of one period, whereas the Sarkar solution lags behind the measurements by approximately half that amount. All three solutions are very similar near the jet exit. However, the amplitude of the first pressure peak near the jet exit is underpredicted by approximately 15 percent.

Figure 14 shows the computed values for the axial turbulence velocity component and the measured data obtained by Seiner, Dash, and Wolf (ref. 26). The interaction between the repeated shock-cell structure and the turbulence produces a significant periodic modulation of the axial turbulence velocity component. The magnitude of the fluctuation is in phase with the pressure fluctuation in the jet. (See fig. 13.) Good agreement in both phase and amplitude is seen between the computed solutions and the measured data. The compressibility-corrected solutions provide better agreement with the measurements than the uncorrected solution. It is encouraging to find from this comparison that the standard Jones-Launder k-ε model is capable of accurate predictions of the turbulence velocity in a shock-containing supersonic jet. For practical applications such as jet noise prediction, an estimate of turbulence intensity in the jet flow is needed. A computational capability for predicting turbulence intensity distributions in the jet flow is highly desirable because measurement of turbulence in high speed flow is exceedingly difficult.

Better predictions of the turbulent velocity fluctuations in a supersonic jet can be obtained with further improvement of the turbulence model. In standard k-ε turbulence models, the local turbulence kinetic energy is attributed equally to all three turbulence velocity components. However, it is known that the magnitude of the axial component is higher than those of the transverse components in the jet shear layer. Therefore, a better redistribution relationship of the turbulent kinetic energy and the Reynolds stress tensor components would raise the value of the computed u_t/U_e. Furthermore, the modulation of the axial turbulence velocity component by the internal shock waves would be stronger, since the amplitude of shock turbulence interaction is roughly proportional to the shock strength and the magnitude of the axial component of the velocity fluctuations.

Use of the space-marching algorithm to obtain a jet flow solution requires less than 100 seconds of CPU time on the Cray Y-MP computer at the Langley Research Center. Use of the time-marching solver to obtain a converged solution for the same cases typically requires 2000 seconds of CPU time. The ratio of computer time required when using the time-marching solver increases by a factor of 20. Figure 15 presents jet centerline pressure distributions obtained by using the space-marching and time-marching solvers. The flow solutions obtained by these two different procedures are practically the same. Detailed discussion of this comparison can be found in reference 27.

Off-Design Supersonic Jets Containing a Mach Disk

Mach disks may appear in a supersonic jet if the operating NPR is significantly different from NPR design value. The conditions for Mach disk formation for a given nozzle depend on nozzle design Mach number and details of the nozzle geometry, such as the nozzle wall exit angle. Mach disk formation can occur in both overexpanded and underexpanded conditions. For a Mach 2.0 nozzle with on-design NPR of 7.82, Mach disk appears if the operating NPR is less than 4.6 or greater than 13.8. For a nozzle with $M = 1.5$ with an on-design NPR value of 3.67, a Mach disk will form in the jet for NPR less than 2.7 or greater than 6.1.

For jet flow computations where Mach disk formation is expected, the time-marching solver in the PAB3D code is used. A different computational grid is also required. When the case of a Mach disk containing jet flow is originally computed with the on-design jet grid, the Mach disk is never formed in the converged solution. The shock front initiated at the nozzle exit propagates as

a weak shock all the way to the jet centerline and then continues as a regular reflected weak shock. In the on-design grid, the cell streamwise versus radial aspect ratio is 4. Although the PAB3D code solver is designed as an upwind algorithm, certain numerical errors in the transonic regime prevent the proper formation of a Mach disk in the flow solution. Because general patched grid capability is available in the PAB3D code, a new grid is created so that the grid for x/R from 0 to 2 has a grid distribution similar to the on-design jet grid but with double the density in each direction. For x/R from 2 to 10, a uniformly sized grid distribution is retained in the streamwise direction. In the radial direction, a uniform grid distribution is provided for y/R from 0 to 2 so that cell aspect ratio in the entire region is 1.0. An exponentially expanding grid is used for y/R from 2 to 8 to cover the free-stream domain outside the jet flow. Figure 16 shows a sketch of this revised grid. The overall grid domain is divided into four blocks for computational convenience. The correct Mach disk containing solution is obtained by using this revised grid.

A solution for a Mach 1.5 jet operating at NPR = 11.6 ($p_e/p_o = 3.15$) is obtained. Figure 17 shows the density and Mach number distributions in the jet. A well-formed Mach disk is located at $x/R = 4.4$. The radius of the Mach disk is approximately $0.68R$ in the computed solution. The location of this Mach disk agrees with the measurements given in reference 5. However, the computed radius of the Mach disk is smaller than the corresponding measured value. The reflected weak shock and a slip line initiated at the outer edge of the Mach disk is clearly shown by the computed density contours. The contour value indicates that the Mach number upstream of the Mach disk has accelerated to values greater than 4.0, whereas the Mach number downstream of the first Mach disk is reduced to values below 0.2. Downstream of the first Mach disk, the flow near the centerline again accelerates to supersonic speeds near $x/R = 8.0$. A second Mach disk is subsequently formed at $x/R = 8.6$. Though much weaker, the second Mach disk can be seen in a schlieren photograph for a jet operating at nearly the same jet initial conditions. (See ref. 5.)

Since the time-marching computations for the Mach disk case are executed by using grid sequencing, converged solutions at three grid levels are obtained during the process. Figure 18 shows the Mach number contours using the one-fourth and one-half linear grid density in the j- and k-directions. Even at the quarter density grid level, the first Mach disk is captured in the solution. Both the location and the radius of this Mach disk are established in this coarse grid. In the half density grid, the second Mach disk emerges in the solution. Only minor changes in the flow physics are detectable between the half density grid solution and the full density grid solution, as shown earlier in figure 17.

Adaptive Grid Computations of Nonaxisymmetric Jets

For jet flow computations using an adaptive grid, a quarter plane symmetry for the jet is assumed. The grid is divided into two domains: a high grid density inner domain near the jet flow, and an outer domain with reduced grid density to cover the free-stream domain away from the jet flow. A Cartesian grid topology is used in the inner domain to accommodate a wide range of jet exit geometries. The outer domain has a polar topology with significantly less grid density than the inner domain. Figure 19 shows a sketch of the grid cross section. Reference 28 shows that the computational simulation of a circular jet remains perfectly axisymmetric even though the grid is Cartesian. Furthermore, the adaptive grid procedure provides adequate grid densities to support accurate computations in the jet shear layer and in regions near a shock front.

This section discusses computed solutions for an elliptic, a rectangular, and a square jet using the adaptive grid method. The elliptic jet is known for its unusual mixing characteristics. The rectangular jet family, which includes the square jet as a special case, is widely used for propulsion integration in advanced aircraft systems. Both elliptic and rectangular jets are capable of switching their major and minor axis directions in different cross sections along the jet. An initial Mach number of 2.0 and an operating NPR of 11.31 are chosen for all three configurations. The operating NPR corresponds to an exit static pressure ratio of $p_e/p_o = 1.445$. In addition, the Mach 2 elliptic jet is also computed at its on-design flow condition at NPR = 7.82.

Figure 20 shows the computed Mach number contours for the underexpanded elliptic jet in the major and the minor planes of symmetry. The elliptic cross section at the nozzle exit plane has an aspect ratio of 2.0. The shock fronts are clearly defined by the Mach number contours in the major plane of symmetry. The shock reflection pattern in the core region of the jet is quite regular. In the plane containing the minor axis, the shock is initially reflected in the shear layer with a scale proportional to the minor axis length. However, the short wave pattern quickly disappears at approximately $x/R = 6$. Farther downstream in the jet, only the long wave pattern dominated by the length scale of the major axis remains. Another unique feature in figure 20 is the expansion rate of the outer jet boundary. In the plane containing the major axis, the jet boundary expands slowly in the radial direction. In contrast, the jet boundary in the plane containing the minor axis expands rapidly in the radial

direction. By approximately $x/R = 15$, the width of the elliptic jet in the original minor axis direction has exceeded the jet width in the original major axis direction. Hence, this computation indicates an axis switching phenomenon for a supersonic elliptic jet.

When using similarity analysis, the major and the minor axes of the initial cross section are considered two independent reference scale lengths for the jet flow. A simple consequence of assuming two independent reference scales would be that the internal shock reflection pattern would repeat in two directions along two different scales. On the other hand, the difference between these two scales must be resolved within the jet flow to a common scale since shock fronts cannot cross each other without some type of interaction. The computed result demonstrates the complexity of such aerodynamic interactions. In the plane of symmetry containing the minor axis, the internal shock wave length is initially governed by the minor axis scale. However, the shear layer position expands rapidly outward in the minor plane of symmetry; thus, the reflection length scale of the downstream shock wave pattern is changed. In the major plane of symmetry, the width of the jet in this plane remains approximately constant; thus, the reference scale of the jet in the minor axis direction is allowed to catch up. The nonlinear interaction within the jet flow eventually leads to a unified scale length for the shock cell system.

Figure 21 shows the Mach number contours in an on-design elliptic jet at Mach 2.0. In the absence of a shock structure in the jet, the Mach number distribution in both the major and minor planes of symmetry is smooth and indistinguishable from the previously computed Mach number distributions in circular jets. Similar to the underexpanded elliptic jet case, the shear layer growth in the minor plane of symmetry is faster than the growth in the major plane of symmetry. At $x/R = 40$, the widths of the jet as seen in both planes of symmetry are almost equal. However, axis switching does not occur in the on-design case.

In order to examine the possibility of axis switching, cross section Mach number contours are shown for these four jets in figures 22–25. The exit cross section aspect ratio for the elliptic and the rectangular jet exit shapes is 2.0. The Mach number contours in each of the cross sections show only a narrow band from $M = 0.8$ to $M = 1.2$ with a contour interval of 0.1 to highlight the shape of the cross section. Figure 22 shows the evolution of the elliptic underexpanded jet cross sections. At the exit, the major axis of the elliptic cross section is oriented in the horizontal direction. The jet boundary grows rapidly in the vertical direction. At $x/R = 30$, the major axis of the elliptic cross section has clearly switched to the vertical direction. The aspect ratio of the ellipse at $x/R = 30$ is approximately 1.50.

Figure 23 shows the equivalent sequence for a rectangular jet. Jet boundary growth in the vertical direction is even faster than that of the elliptic jet. At $x/R = 30$, the aspect ratio of the shape is approximately 1.70. The corners of the original rectangular shape have been rounded off in the process of turbulent mixing.

Figure 24 shows the evolution sequence for a square jet. In this case, the original square shape for the Mach number contours evolves rapidly in the jet flow. At $x/R = 12$, the corners of the square are actually transposed by 45°, with the corner sharpness well preserved. As the shear layer grows thicker farther downstream, the shape of the jet cross section quickly losses its distinction as a square and eventually becomes circular.

Figure 25 shows the shape evolution sequence for an elliptic jet with on-design exit pressure ratio. Although the jet grows mainly in the vertical direction, axis switching does not occur in this on-design jet flow. The jet simply becomes a near-circular jet at $x/R = 30$. At the last computed streamwise position at $x/R = 40$, the cross sections for all four jets simply retain their geometrical characters similar to those established at $x/R = 30$.

Figure 26 shows the Mach number contours in the plane of symmetry of the square jet and its centerline Mach number distribution. Qualitatively, these distributions are very similar to the corresponding distributions shown in figure 27 for a circular jet operating at the same exit Mach number and NPR. The visually striking dynamic behavior of the square jet axis (fig. 24) shows that switching apparently has little influence on flow development near the jet centerline. It should be pointed out that the square jet and the circular jet, with a common reference dimension of 1.0, have different jet exit areas. In order to compare the streamwise jet flow development on a normalized basis, the length scale for the square jet in figure 24 should be reduced by a factor of $\sqrt{\pi/4} = 0.8862$. With this scale adjustment, the phase and amplitude of the centerline Mach number oscillations of the square jet and the circular jet agree almost exactly starting from the second peak.

In order to provide some validation for the adaptive grid computation procedure for nonaxisymmetric jets, a Mach 2.0 on-design circular jet solution computed by using the axisymmetric grid is compared with the same jet computed by using a three-dimensional adaptive grid. Two levels of adaptive grid densities are also used to verify grid convergence: 40×40 cells and 56×56 cells for the inner high density grid cross sections. Figure 28 shows the axisymmetric grid solution for $M = 2.0$. The adaptive grid results are shown in figures 29 and 30.

Nearly identical solutions for the turbulence intensity distribution in the meridian plane and along the centerline of the jet are obtained for the two adaptive grid densities. For example, the maximum turbulence level in the jet plume is 0.134 for both the 40×40 cell and the 56×56 cell solutions. The solution using an axisymmetric grid differs slightly from the adaptive grid results in two aspects. First, the maximum turbulence level in the middle of the shear layer is slightly higher, with a value of 0.142. Second, the turbulence intensity profile along the centerline is shifted upstream by approximately $x/R = 2.0$.

The reason for the different maximum intensity in the shear layer is not clear. However, the spatial shift of the turbulence intensity profile along the centerline has a geometrical explanation. It is difficult for the grid adaption algorithm to handle very large velocity gradients such as those occurring near the jet exit. Consequently, it is not possible to specify an initial shear layer thickness of less than 0.05 jet radius at the jet exit plane. Since the initial shear layer is thicker, the inner boundary of the turbulent shear layer intersects with the centerline at a smaller value of x/R. In fact, with a downstream shift of the adaptive grid centerline turbulence intensity profile, the turbulence intensity profile can be matched perfectly with results using the axisymmetric grid.

Concluding Remarks

The main purpose of this report is to establish a unified method for jet flow prediction using the Navier-Stokes method with a two-equation k-ε turbulence closure model. Although the jet flow may contain a variety of complex flow physics features, the Navier-Stokes method simply requires that the initial condition and boundary conditions of the jet operating conditions be specified for the problem. Detailed flow physics developments in the jet are predicted by the Navier-Stokes method. The validity of this approach is demonstrated by the high quality jet flow solutions obtained with the PAB3D code.

This study examines several categories of jet flow conditions. For on-design subsonic and supersonic axisymmetric jets, the flow field is dominated entirely by turbulent mixing. Numerical solutions within a Mach number range of 0.6 to 3.0 are accurate when compared with available experiment data for parameters such as mean velocity and turbulence intensity distributions in the jet, centerline velocity decay, and the potential core length variation as a function of Mach number.

For off-design supersonic jet flows containing weak shocks, flow predictions are compared with experimental data. Good agreement is obtained between the computed results and experimental data for key parameters, including first shock-cell lengths and centerline pressure distribution. The predicted distributions of the streamwise component of turbulence velocity fluctuation in an underexpanded Mach 2.0 jet show good agreement with measured data.

Turbulence intensity in the jet flow is an important quantity for jet noise prediction. Since direct measurement of turbulence in a supersonic jet is very difficult to make, a predictive capability provided by the PAB3D code is very useful for practical applications. Good agreement between predictions and experimental measurements has also been obtained for a Mach 1.5 jet operating at 3.15 times its design nozzle pressure ratio where Mach disks are present in the jet flow.

Many of the modern propulsion jet nozzles employ nonaxisymmetrical exit geometries. The adaptive grid method examined in this study has produced good results for elliptic, rectangular, and square jets. However, the computed results are not verified for lack of experimental data. The accuracy of the adaptive grid procedure is illustrated by a comparison between an adaptive grid solution of an axisymmetric jet and a solution for the same jet using a single cell wedge grid. Although the adaptive grid has a Cartesian-topology and the single-cell wedge grid has cylindrical symmetry boundary conditions, the solutions are essentially identical.

For most jet flows where strong shocks are absent in the computational domain, the space-marching solver in the PAB3D code can be used. When the space-marching option is used for jet flow computation as conditions permit, the computer time is one twentieth of the time required for obtaining a time-marching solution with the same flow conditions. The accuracy of the solutions obtained by these different solvers is practically indistinguishable. Substantial savings in computer time can be realized by using the space-marching method in the PAB3D code if the analyses of many cases of jet flow conditions are required for design applications.

NASA Langley Research Center
Hampton, VA 23681-0001
May 23, 1996

References

1. Reichardt, Hans: *Gesetzmässigkeiten der freien Turbulenz*. VDI-Forschungsh. 414, 1942.

2. Görtler, H.: Berechnug von Aufgaben der freien Turbulenz auf Grund eines neuen Näherungsansatzes. *Z. Angew. Math. Mech.*, Bd. 22, Nr. 5, Oct. 1942, pp. 244–254.

3. Warren, Walter R., Jr.: *An Analytical and Experimental Study of Compressible Free Jets*. Publ. No.: 23,885, Univ. Microfilms, Inc., 1957.

4. Abramovich, G. N.: *The Theory of Turbulent Jets*. M.I.T. Press, 1963.

5. Love, Eugene S.; Grigsby, Carl E.; Lee, Louise P.; and Woodling, Mildred J.: *Experimental and Theoretical Studies of Axisymmetric Free Jets*. NASA TR R-6, 1959. (Supersedes NACA RM L54L31 by Love and Grigsby; RM L55J14 by Love; RM L56G18 by Love, Woodling, and Lee; and TN 4195 by Love and Lee.)

6. Dash, Sanford M.; and Wolf, David E.: *Fully-Coupled Analysis of Jet Mixing Problems, Part I: Shock-Capturing Model, SCIPVIS*. NASA CR-3716, 1984.

7. Dash, Sanford M.; Pergament, Harold S.; and Thorpe, Roger D.: *Computational Models for the Viscous/Inviscid Analysis of Jet Aircraft Exhaust Plumes*. NASA CR-3289, 1980.

8. Seiner, John M.: Advances in High Speed Jet Aeroacoustics. AIAA-84-2275, Oct. 1984.

9. Seiner, J. M.; and Norum, T. D.: Aerodynamic Aspects of Shock Containing Jet Plumes. AIAA-80-0965, June 1980.

10. Abdol-Hamid, Khaled S.; and Wilmoth, Richard G.: Multiscale Turbulence Effects in Underexpanded Supersonic Jets. *AIAA J.*, vol. 27, Mar. 1989, pp. 315–322.

11. Abdol-Hamid, Khaled S.: The Application of 3D Marching Scheme for the Prediction of Supersonic Free Jets. *AIAA/ ASME/SAE/ and ASEE 25th Joint Propulsion Conference*, July 1989. (Available as AIAA-89-2897.)

12. Abdol-Hamid, Khaled S.; Uenishi, Kenji; and Turner, William: Three-Dimensional Upwinding Navier-Stokes Code With k-ε Model for Supersonic Flows. AIAA-91-1669, June 1991.

13. Jones, W. P.; and Launder, B. E.: The Prediction of Laminarization With a Two-Equation Model of Turbulence. *Int. J. Heat & Mass Transf.*, vol. 15, no. 2, Feb. 1972, pp. 301–314.

14. Abdol-Hamid, Khaled S.; Lakshmanan, B.; and Carlson, John R.: *Application of Navier-Stokes Code PAB3D With k-ε Turbulence Model to Attached and Separated Flows*. NASA TP-3480, 1995.

15. Eiseman, Peter R.: Alternating Direction Adaptive Grid Generation. *AIAA J.*, vol. 23, no. 4, Apr. 1985, pp. 551–560.

16. Sarkar, S.; Erlebacher, G.; Hussaini, M. Y.; and Kreiss, H. O.: The Analysis and Modelling of Dilatational Terms in Compressible Turbulence. *J. Fluid Mech.*, vol. 227, June 1991, pp. 473–493.

17. Wilcox, David C.: Progress in Hypersonic Turbulence Modeling. AIAA-91-1785, June 1991.

18. Eiseman, Peter R.; and Erlebacher, Gordon: *Grid Generation for the Solution of Partial Differential Equations*. NASA CR-178365, ICASE Rep. No. 87-57, 1987.

19. Eiseman, Peter R.: Adaptive Grid Generation. *Comput. Methods Appl. Mech. & Eng.*, vol. 64, nos. 1–3, Oct. 1987, pp. 321–376.

20. Eiseman, P.; and Bockelie, M.: The Control and Application of Adaptive Grid Movement. *Finite Element Analysis in Fluids, Proceedings of the Seventh International Conference on Finite Element Methods in Flow Problems*, Univ. of Alabama in Huntsville Press, 1989, pp. 1025–1032.

21. Pao, S. Paul; and Abdol-Hamid, Khaled S.: Application of a New Adaptive Grid for Aerodynamic Analysis of Shock Containing Single Jets. AIAA-90-2025, July 1990.

22. Wygnanski, I.; and Fiedler, H.: Some Measurements in the Self-Preserving Jet. *J. Fluid Mech.*, vol. 38, pt. 3, Sept. 18, 1969, pp. 577–612.

23. Eggers, James M.: *Velocity Profiles and Eddy Viscosity Distributions Downstream of a Mach 2.22 Nozzle Exhausting to Quiescent Air*. NASA TN D-3601, 1966.

24. Lau, Jark C.; Morris, Philip J.; and Fisher, Michael J.: Measurements in Subsonic and Supersonic Free Jets Using a Laser Velocimeter. *J. Fluid Mech.*, vol. 93, pt. 1, July 12, 1979, pp. 1–27.

25. Abdol-Hamid, Khaled S.: Three-Dimensional Calculations for Underexpanded and Overexpanded Supersonic Jet Flows. AIAA-89-2196, July–Aug. 1989.

26. Seiner, J. M.; Dash, S. M.; and Wolf, D. E.: Analysis of Turbulent Underexpanded Jets, Part II: Shock Noise Features Using SCIPVIS. *AIAA J.*, vol. 23, no. 5, May 1985, pp. 669–677.

27. Abdol-Hamid, Khaled S.: The Application of 3D Marching Scheme for the Prediction of Supersonic Free Jets. AIAA-89-2897, July 1989.

28. Pao, S. Paul; and Abdol-Hamid, Khaled S.: Application of a New Adaptive Grid for Aerodynamic Analysis of Shock Containing Single Jets. AIAA-90-2025, July 1990.

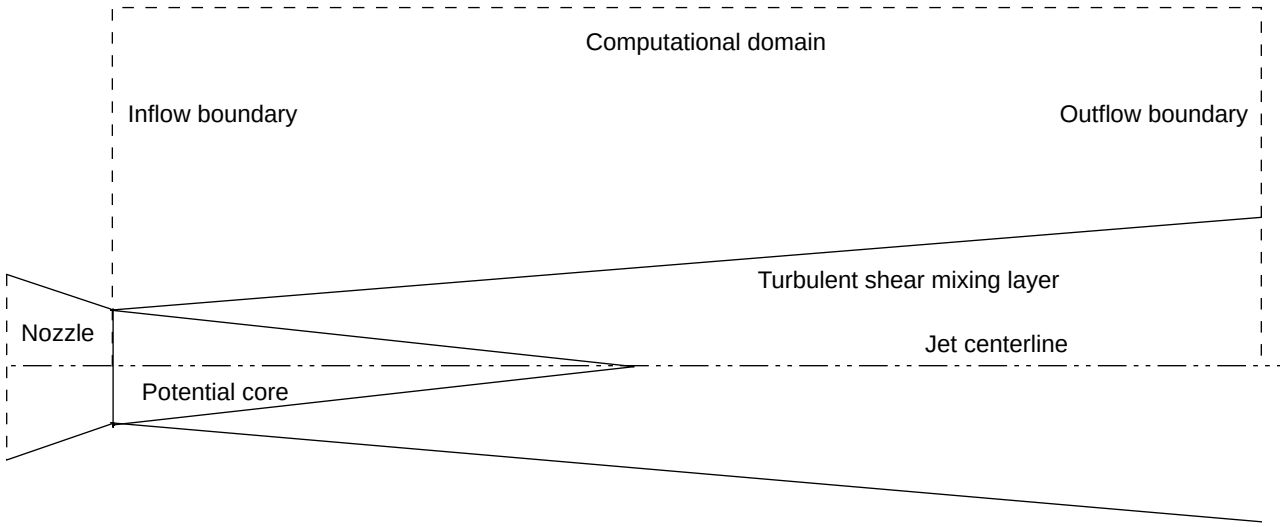

(a) Typical on-design jet flow configuration and terminology.

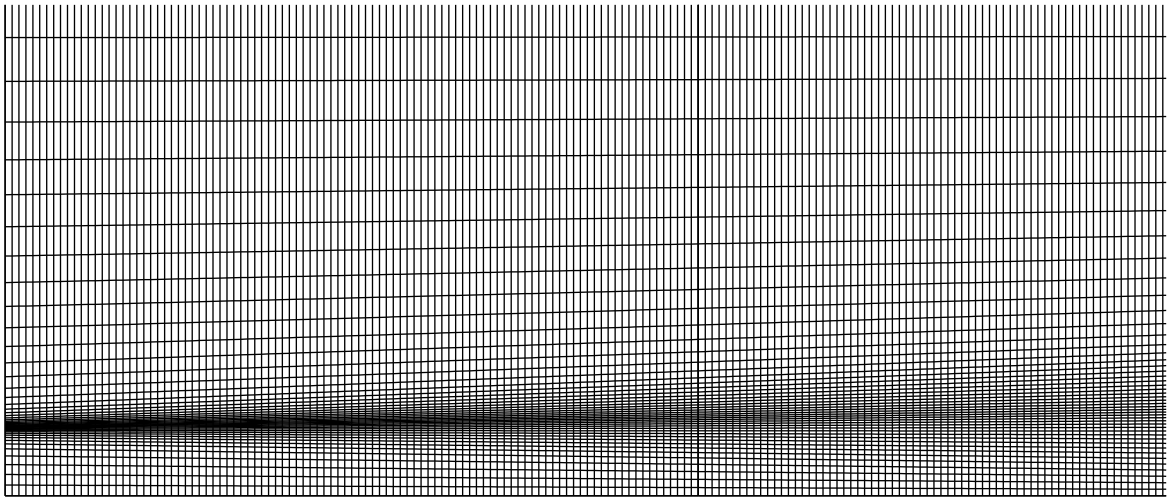

(b) Single cell wedge grid for on-design jet flow computations.

Figure 1. Sketch of typical axisymmetric on-design jet flow and computational grid.

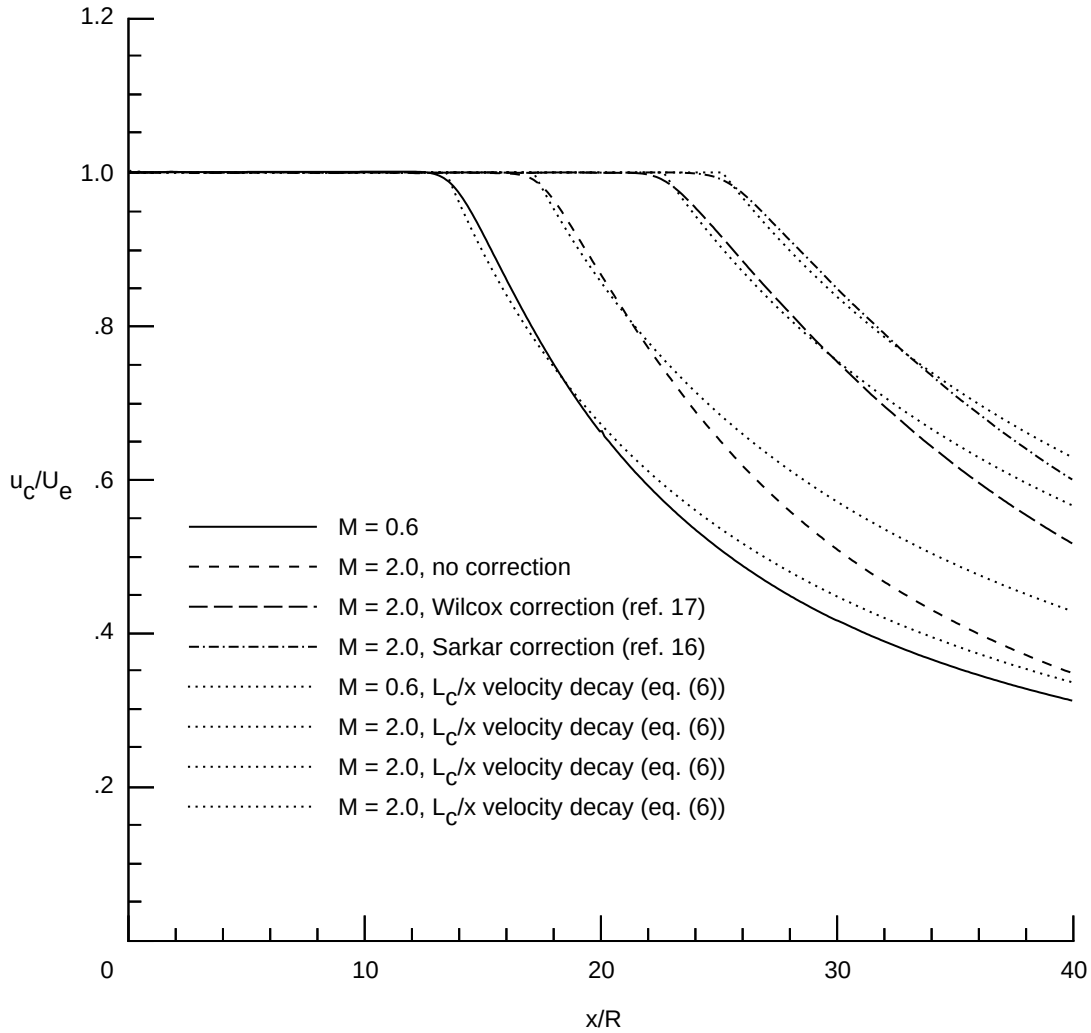

Figure 2. Centerline velocity decay for subsonic and supersonic jet flows computed with standard Jones-Launder *k*-ε turbulence model with different compressibility corrections.

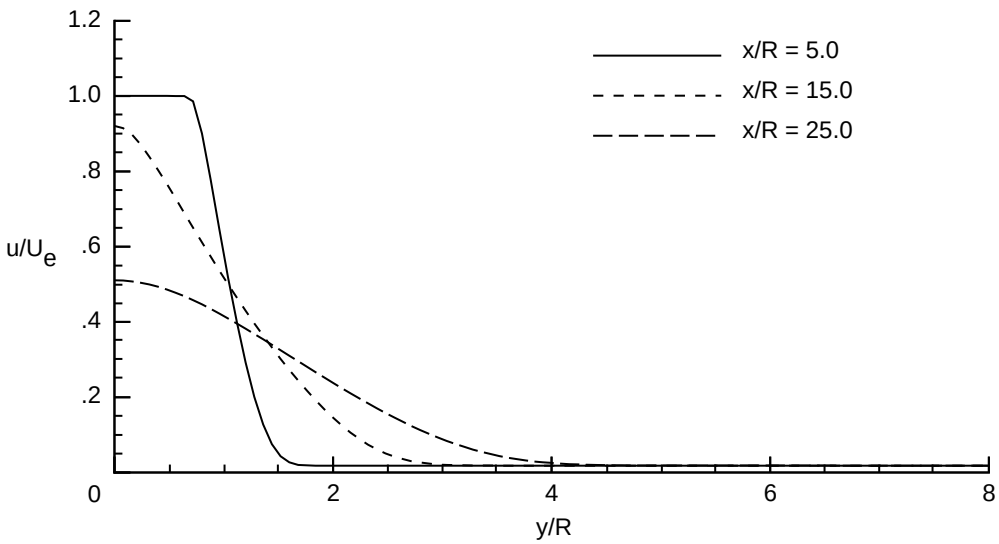

Figure 3. Axial velocity component distribution in cross sections in Mach 0.6 circular jet flow.

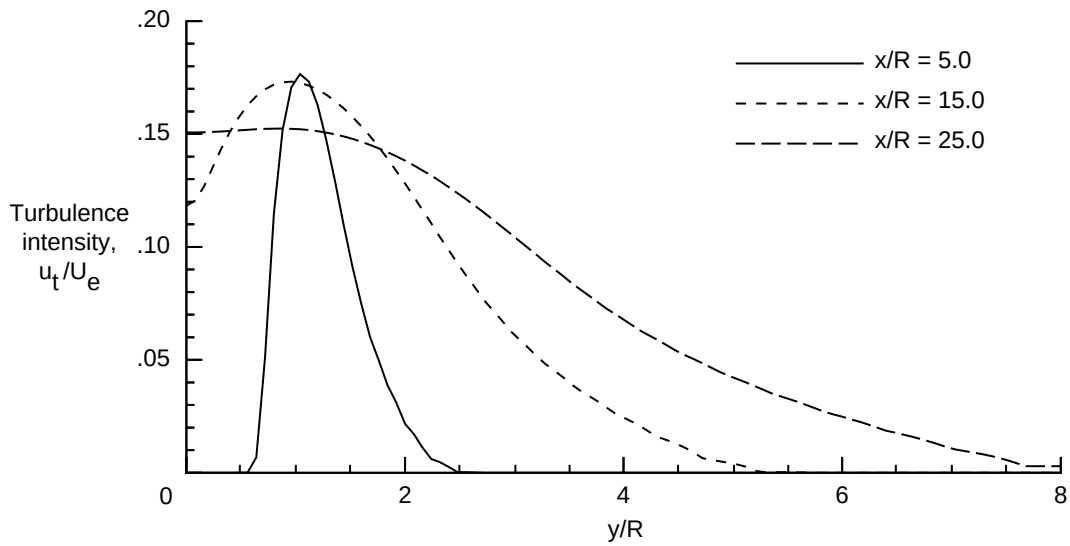

Figure 4. Turbulence intensity distribution in cross sections in Mach 0.6 circular jet flow.

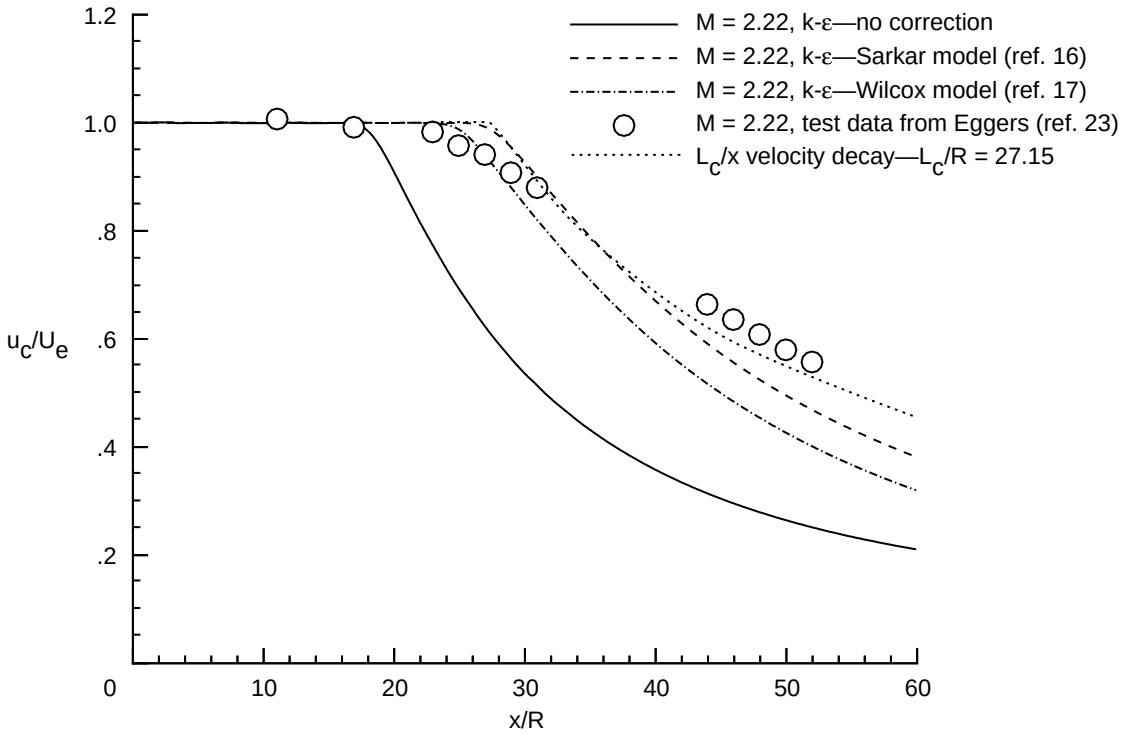

Figure 5. Centerline velocity distribution for supersonic jet using *k*-ε turbulence model with different compressibility corrections.

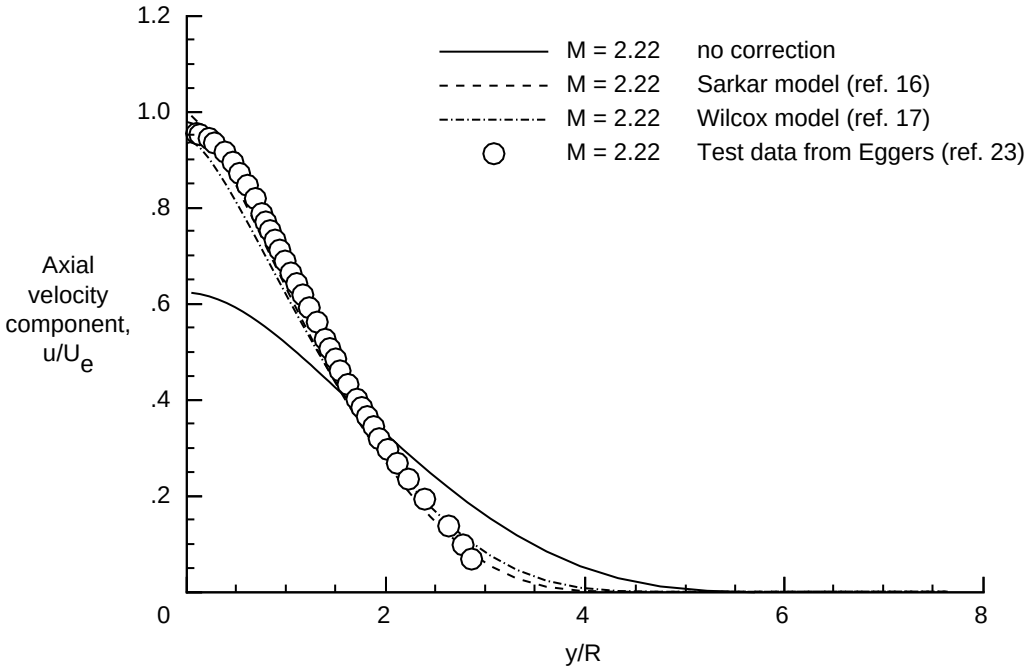

Figure 6. Axial velocity component distribution along radial direction at $x/R = 25$ using *k*-ε turbulence model with different compressibility corrections.

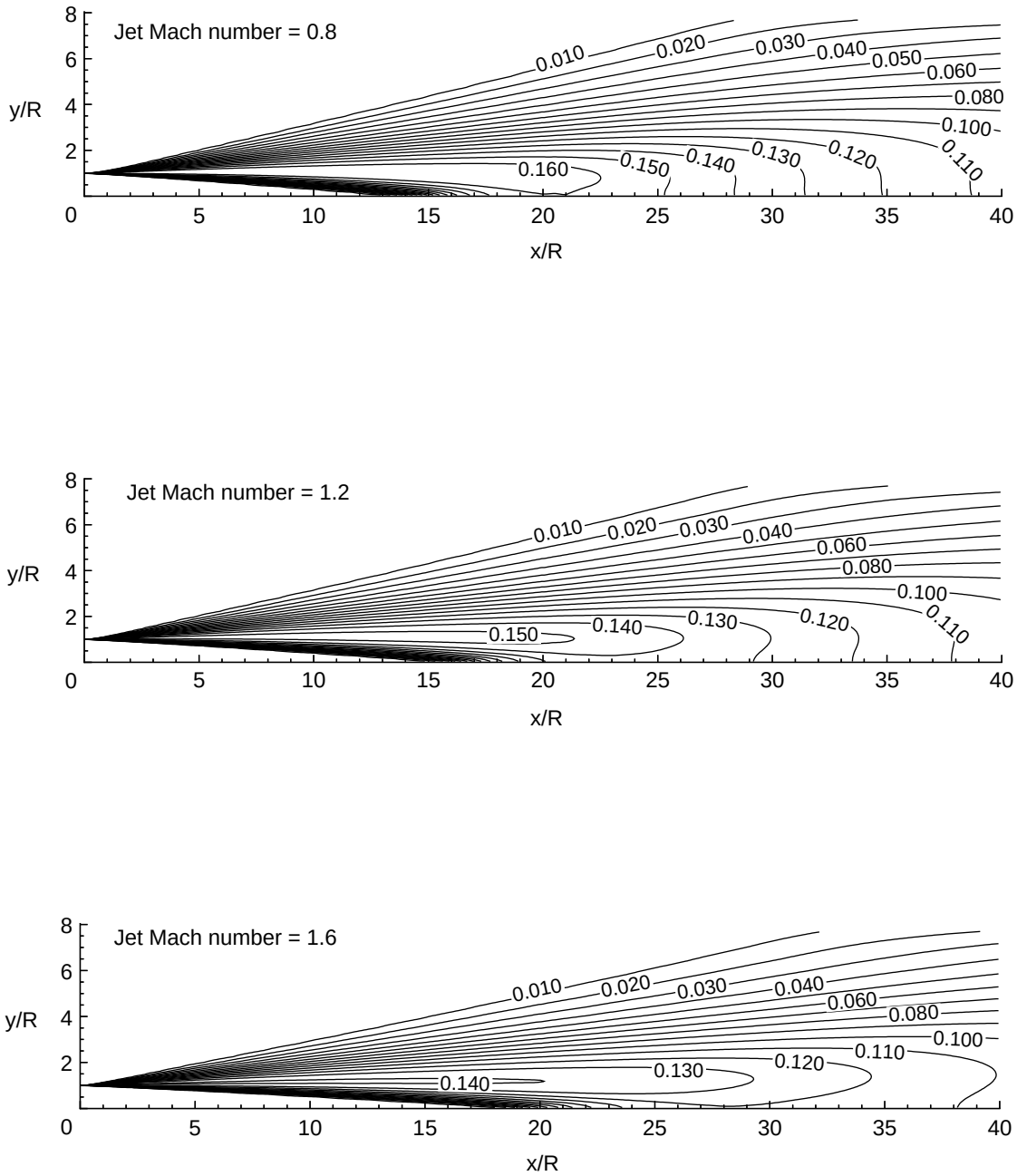

Figure 7. Typical turbulence intensity distribution in axisymmetric jets computed by using Jones-Launder k-ε turbulence model with Wilcox model of compressibility correction for u_t/U_e contours.

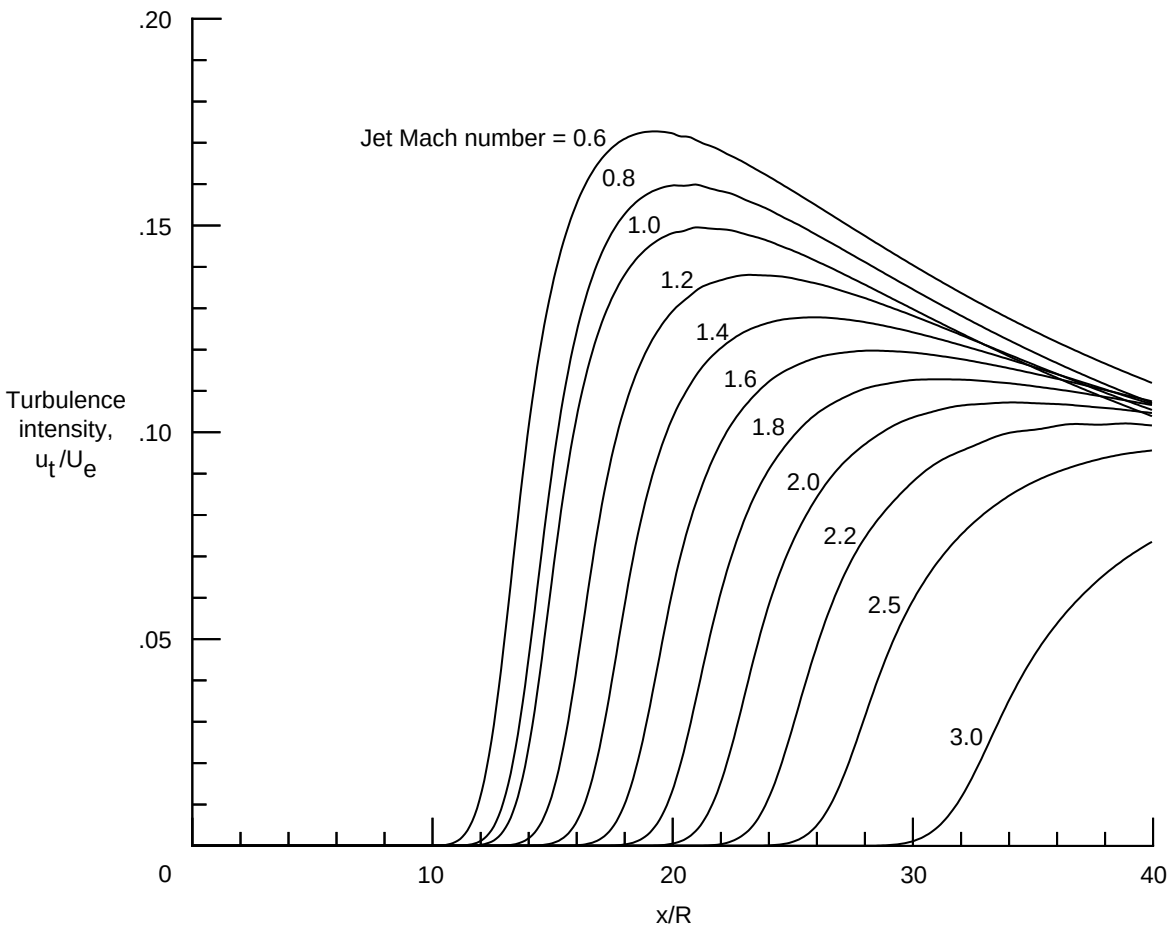

Figure 8. Centerline turbulence intensity profiles of axisymmetric jets at various subsonic and supersonic Mach numbers computed by using Jones-Launder two-equation *k*-ε turbulence model with Wilcox compressibility correction.

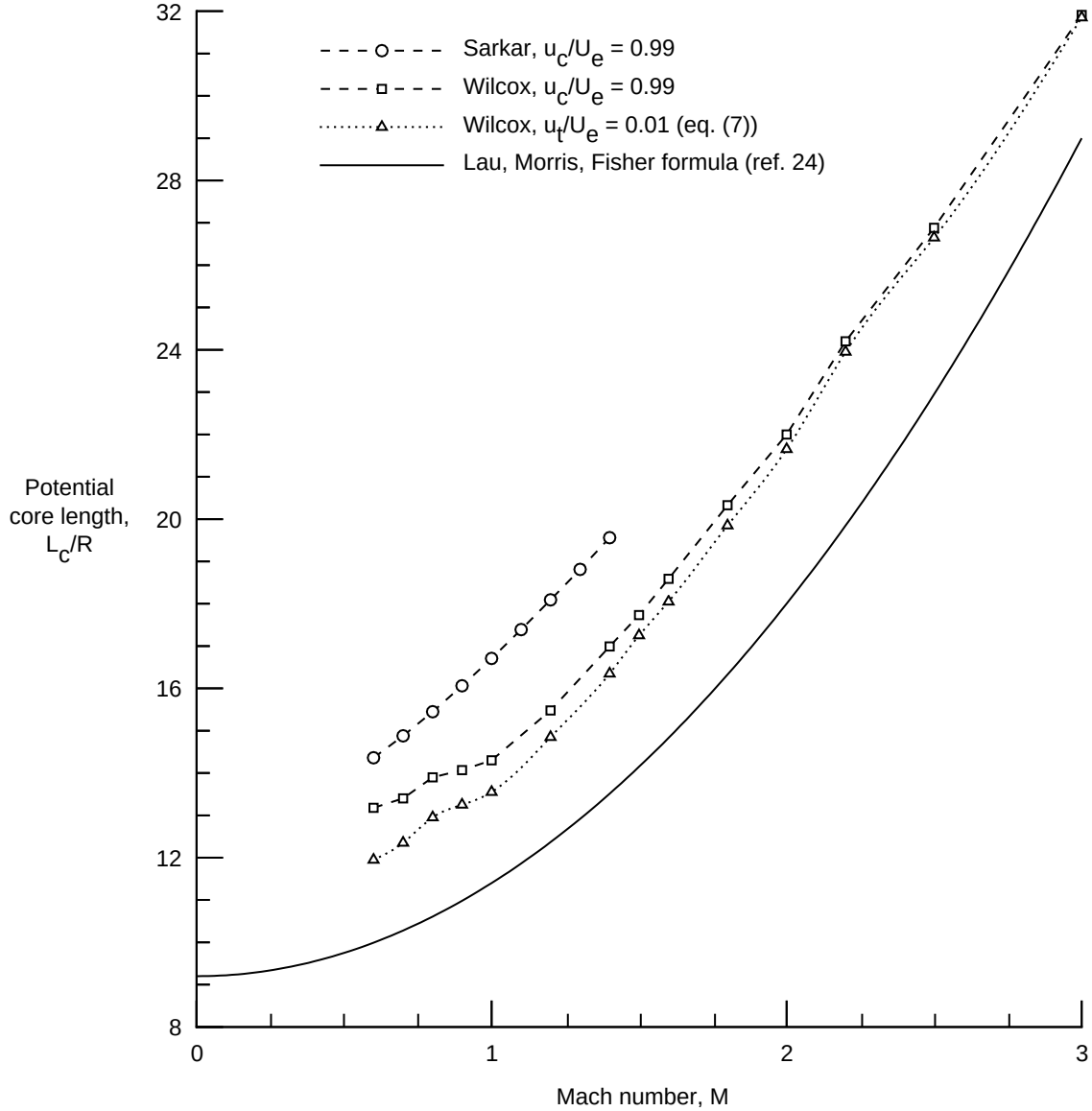

Figure 9. Potential core length as function of Mach number for subsonic and supersonic jets computed with Jones-Launder k-ε turbulence model and different compressibility corrections.

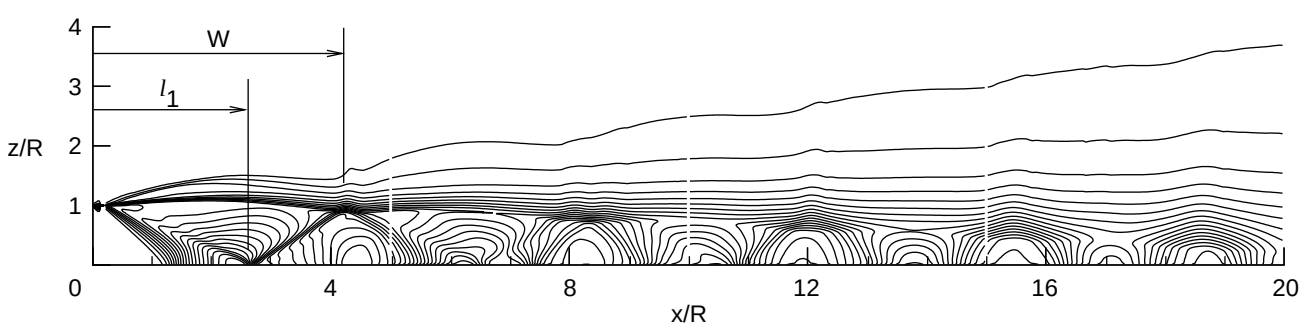

Figure 10. Typical density contours and first shock-cell length definitions for circular underexpanded supersonic jet. Jet exit Mach number = 1.50; p_e/p_o = 1.445.

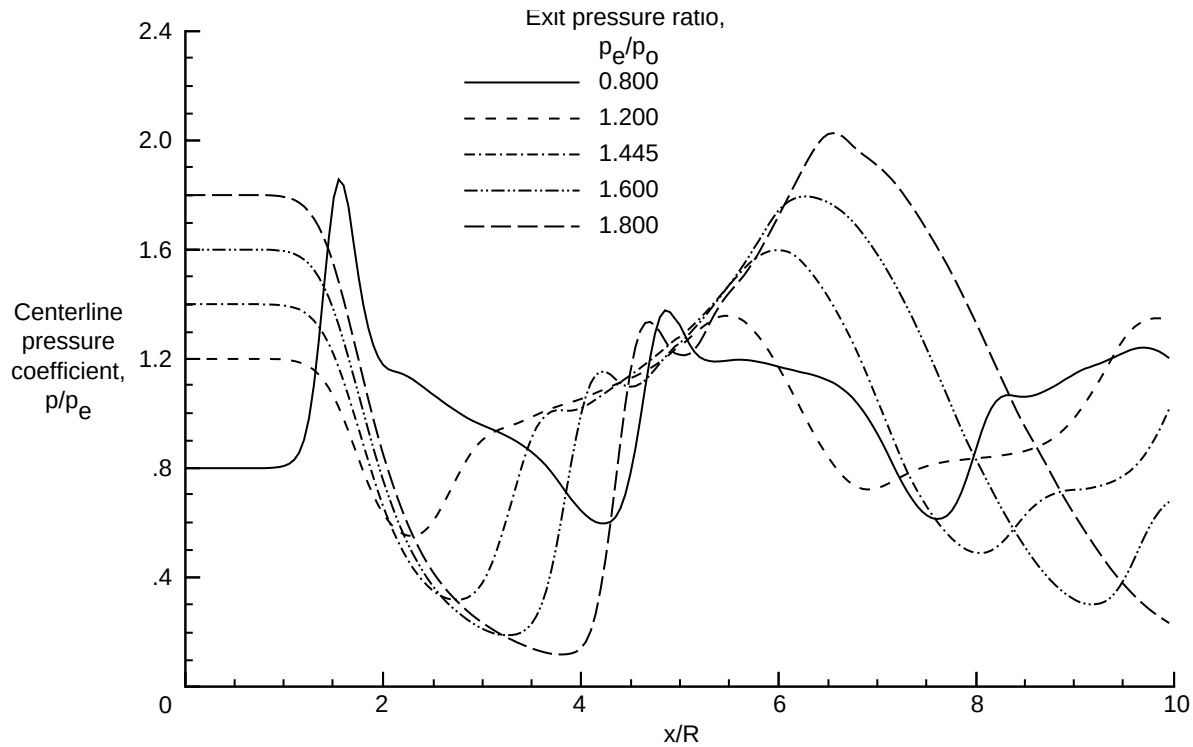

Figure 11. Computed centerline pressure distribution with different exit pressure ratios for Mach 2.0 jet computed with Jones-Launder *k*-ε turbulence model.

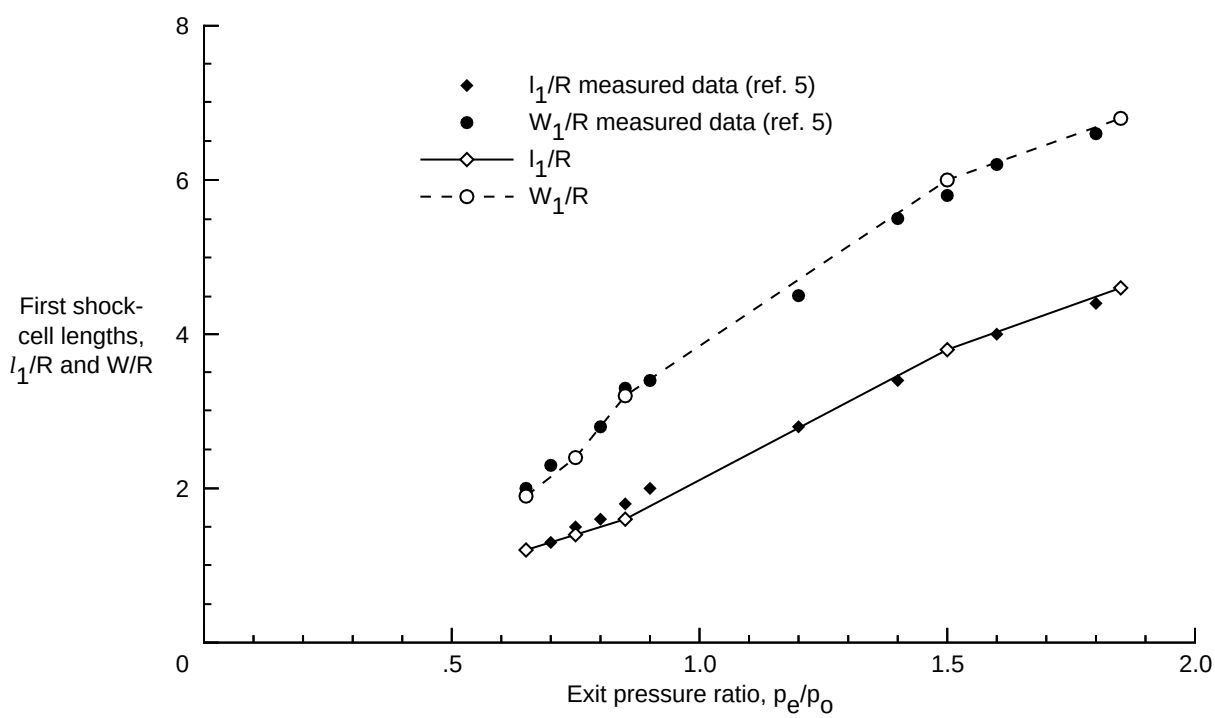

Figure 12. Computed and measured first shock-cell lengths for Mach 2.0 jet computed with Jones-Launder *k*-ε turbulence model.

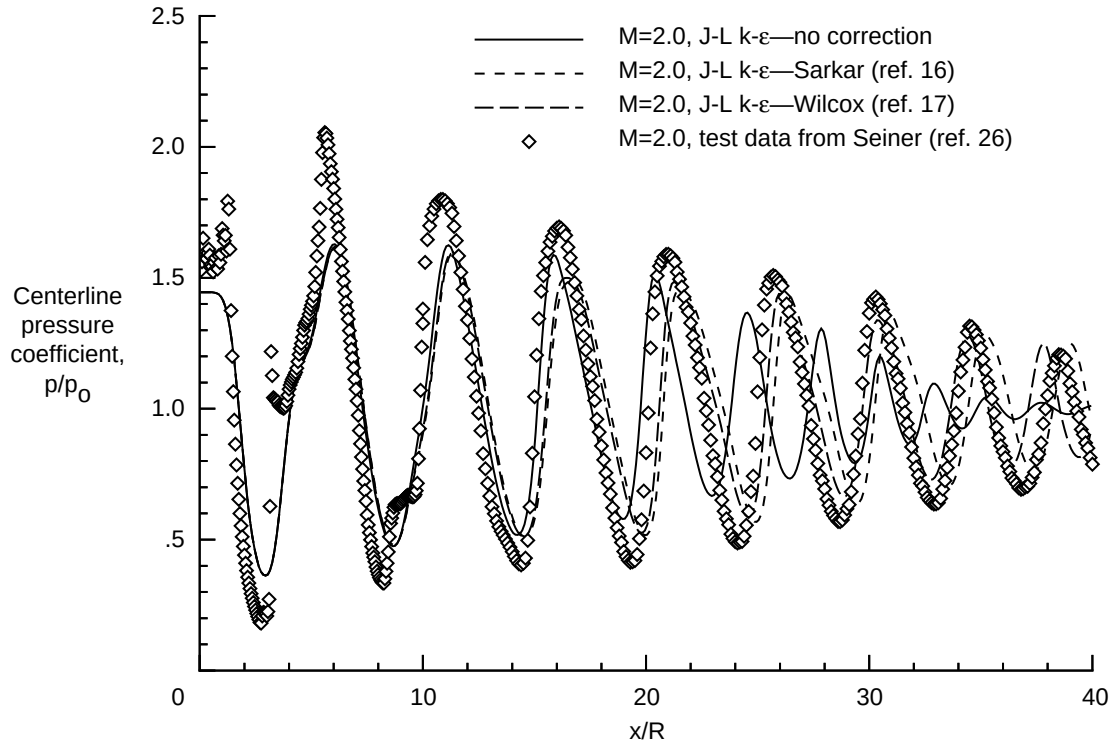

Figure 13. Centerline pressure distribution computed with Jones-Launder *k*-ε model with different compressibility corrections for $p_e/p_o = 1.445$.

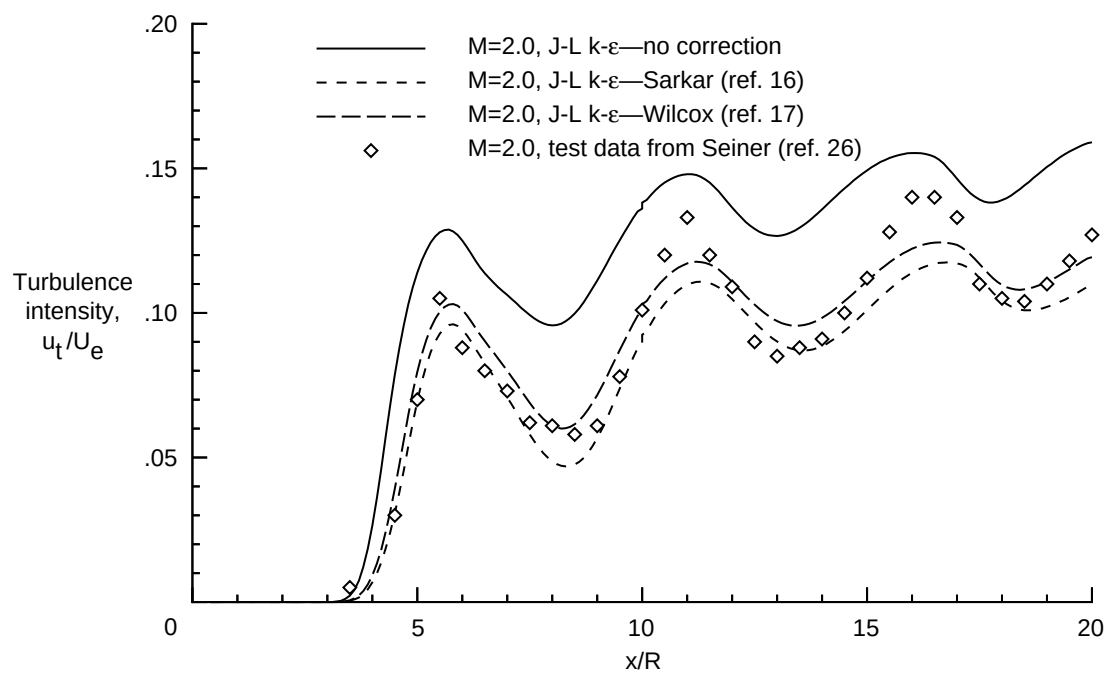

Figure 14. Centerline turbulence intensity computed with Jones-Launder *k*-ε model with different compressibility corrections for $p_e/p_o = 1.445$.

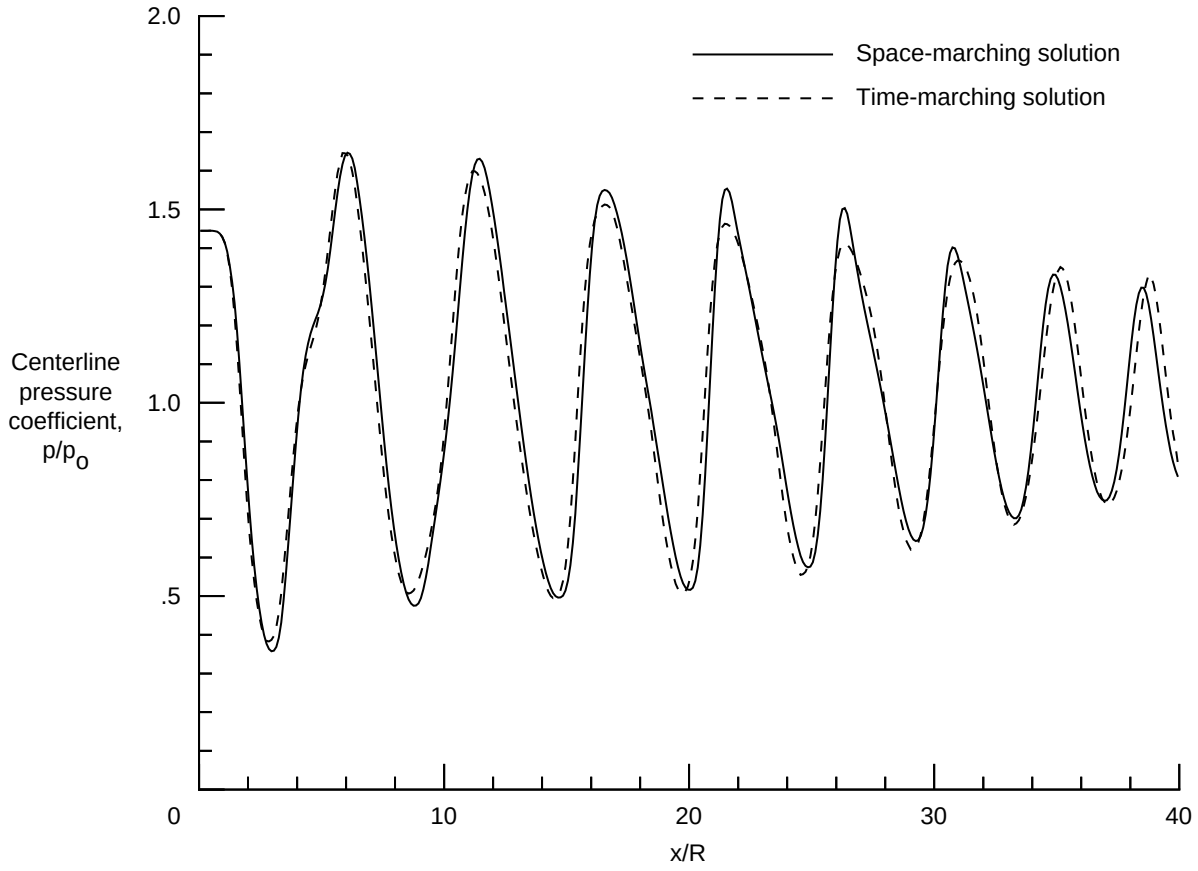

Figure 15. Space-marching and time-marching solutions for underexpanded Mach 2.0 supersonic jet computed with Jones-Launder *k*-ε turbulence model.

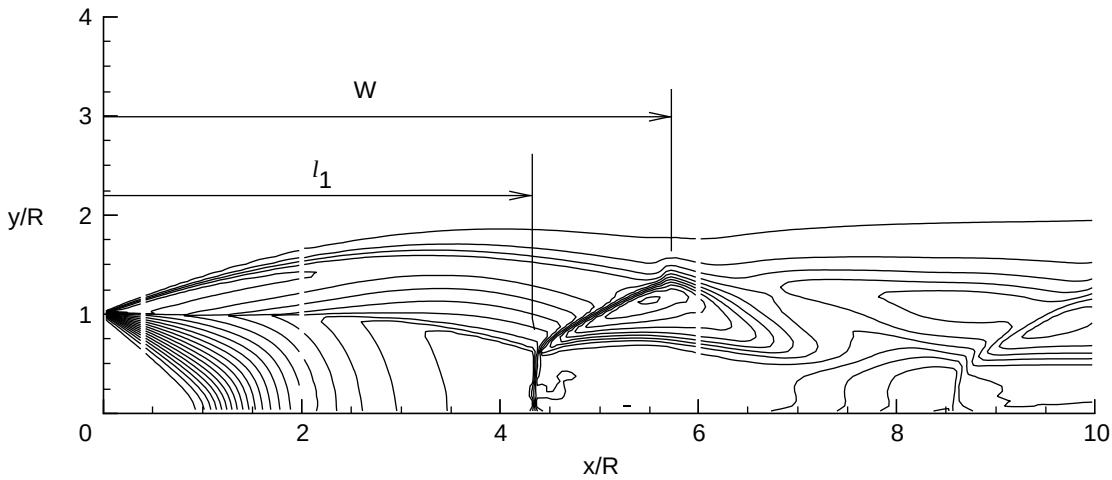

(a) Mach number contours of typical underexpanded supersonic jet containing multiple Mach disks.

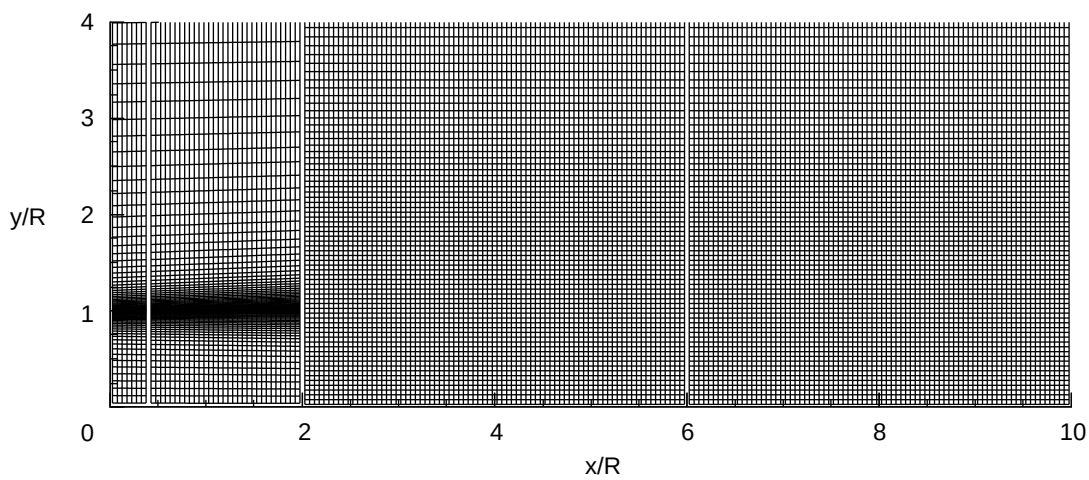

(b) Multiblock single cell wedge grid for jet flows containing multiple Mach disks.

Figure 16. Flow configuration and computational grid for underexpanded jet containing one or more Mach disks.

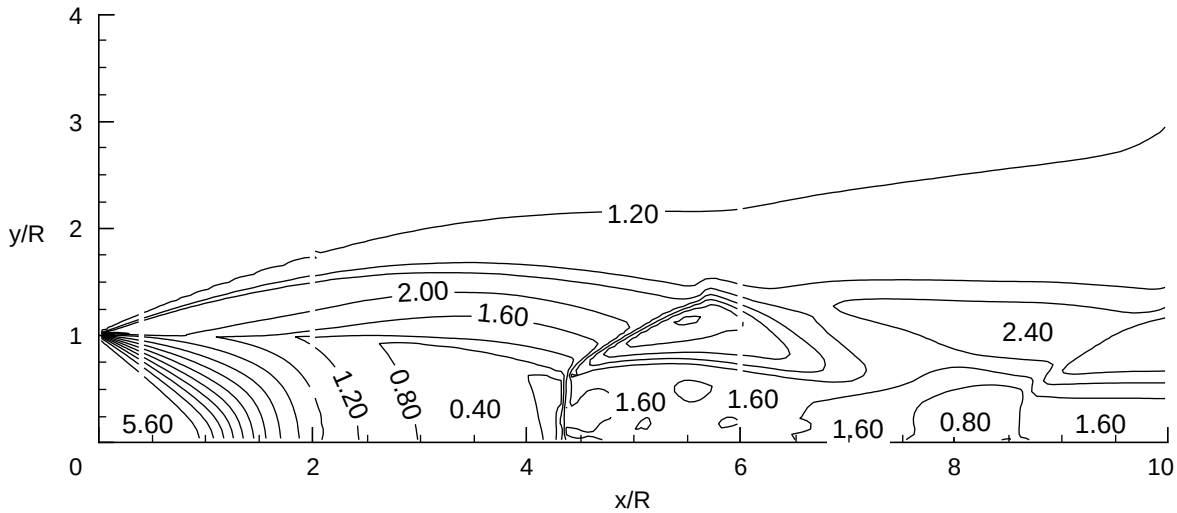

(a) Density contours; Interval = 0.40 kg/m^3.

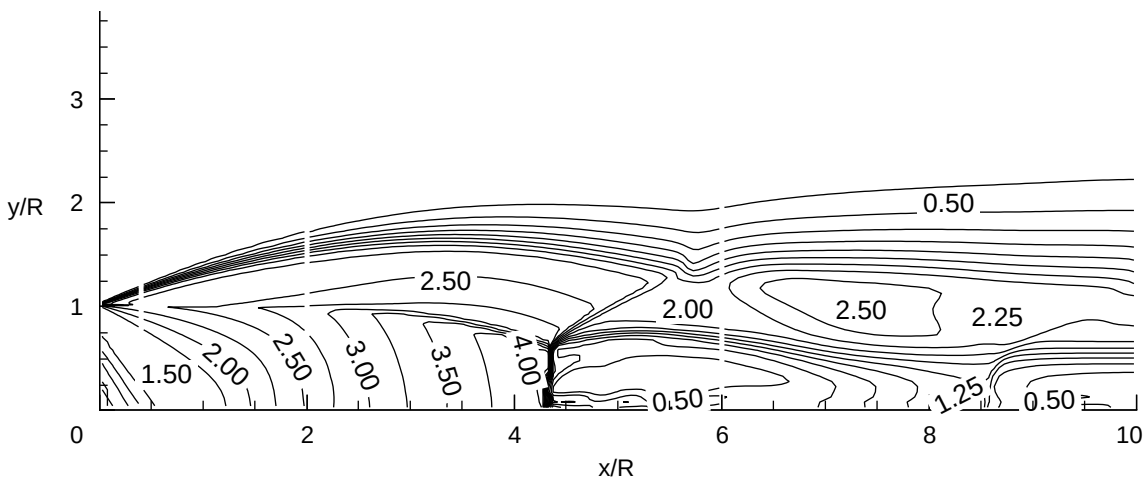

(b) Mach number contour; Interval = 0.25.

Figure 17. Density and Mach number contours for underexpanded circular jet containing multiple Mach disks. Exit Mach number = 1.50; p_e/p_o = 3.15; fine grid solution.

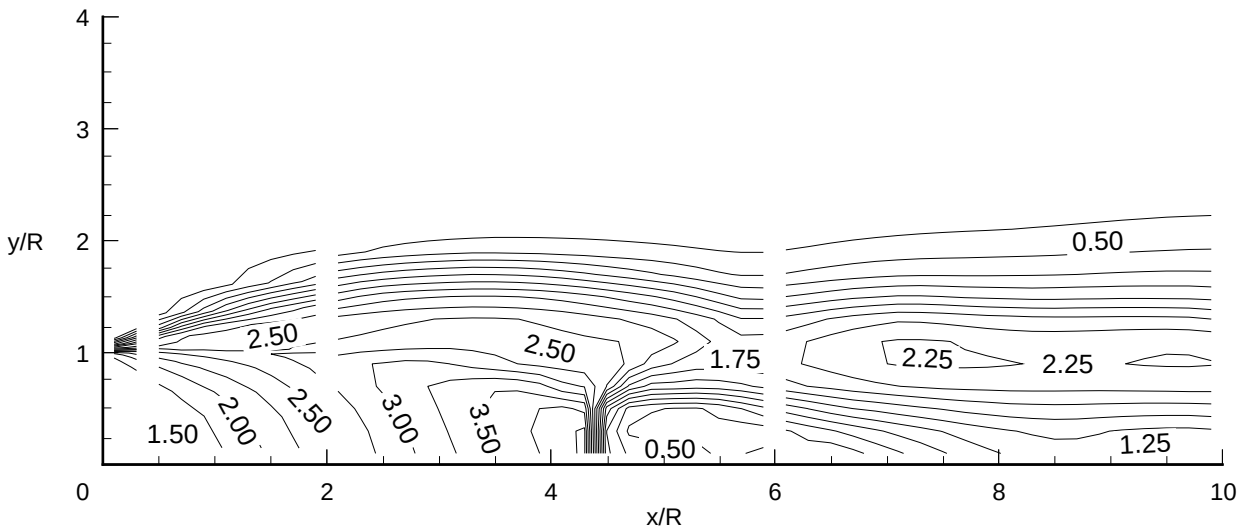

(a) One-fourth density grid Mach number contours; Interval = 0.25.

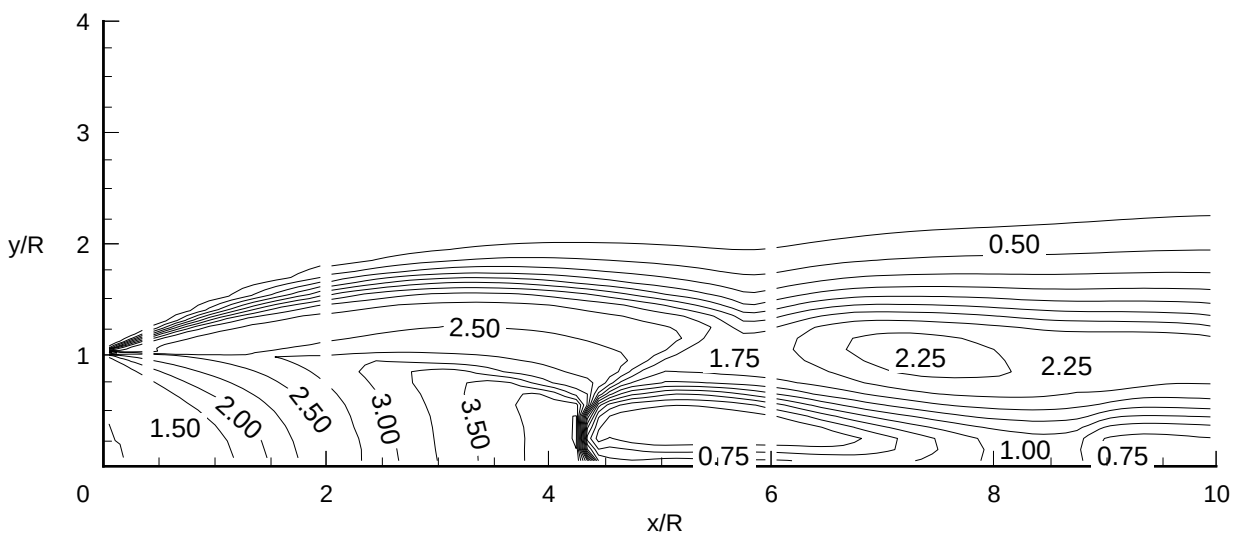

(b) One-half density grid Mach number contours; Interval = 0.25.

Figure 18. Grid study for underexpanded circular jet containing multiple Mach disks. Jet exit Mach number = 1.50; p_e/p_o = 3.15.

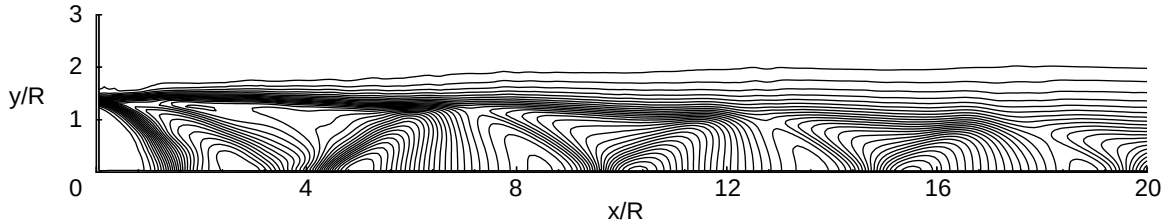

(a) Typical density contours of underexpanded elliptic jet in major plane of symmetry.

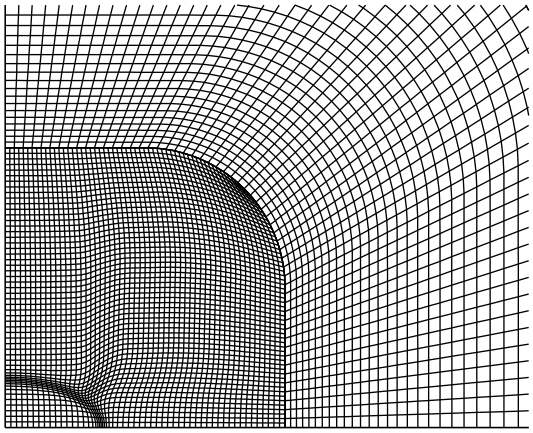

(b) Adapted grid cross section at inflow plane.

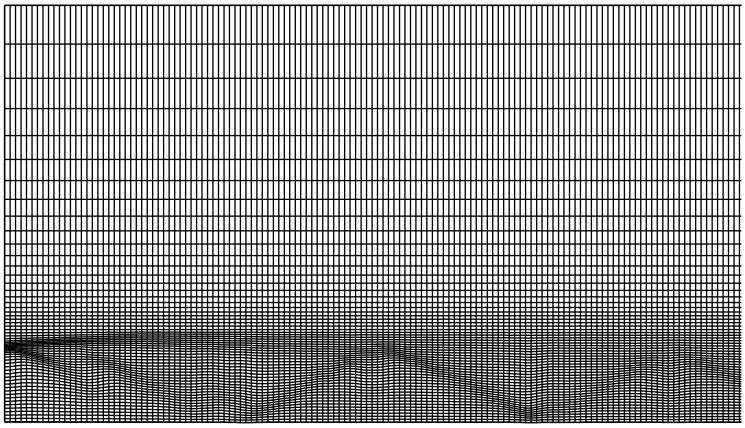

(c) Adapted grid longitudinal profile in plane of symmetry containing major axis of initial jet cross section.

Figure 19. Adapted grid geometry for elliptic supersonic jet. Shape aspect ratio = 2.0.

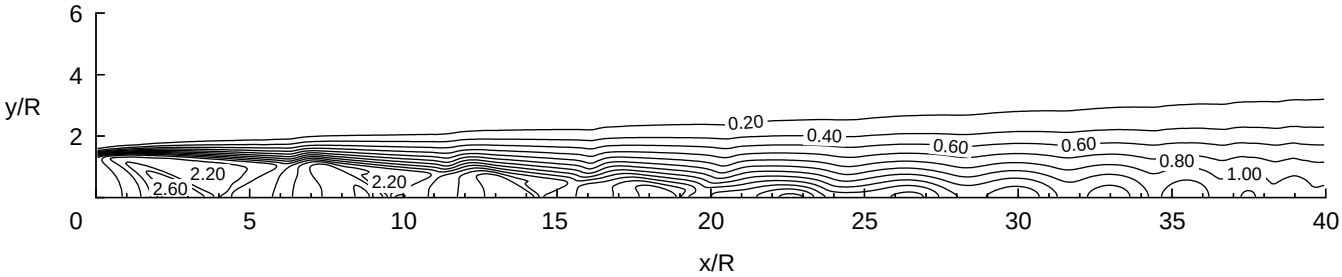

(a) Plane of symmetry containing major axis; Interval = 0.20.

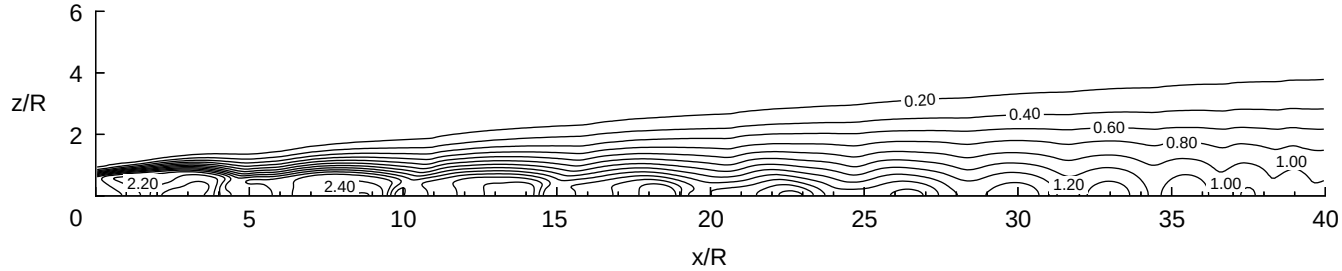

(b) Plane of symmetry containing minor axis; Interval = 0.20.

Figure 20. Mach number contours for underexpanded supersonic jet with elliptic exit cross section. Shape aspect ratio = 2.0; Exit Mach number = 2.00; NPR = 11.12; p_e/p_o = 1.445.

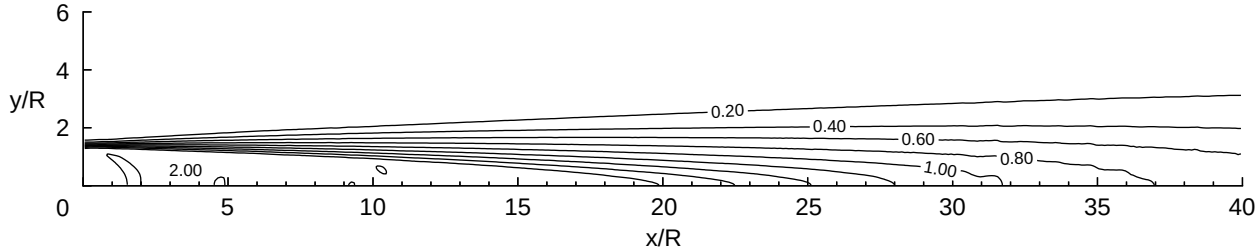

(a) Plane of symmetry containing major axis; Interval = 0.20.

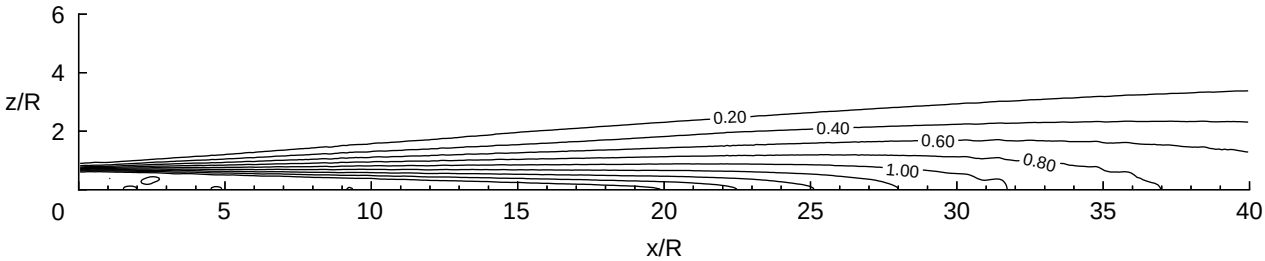

(b) Plane of symmetry containing minor axis; Interval = 0.20.

Figure 21. Mach number contours in major and minor planes of symmetry of elliptic jet shape ratio of 2.0; On-design NPR = 7.82.

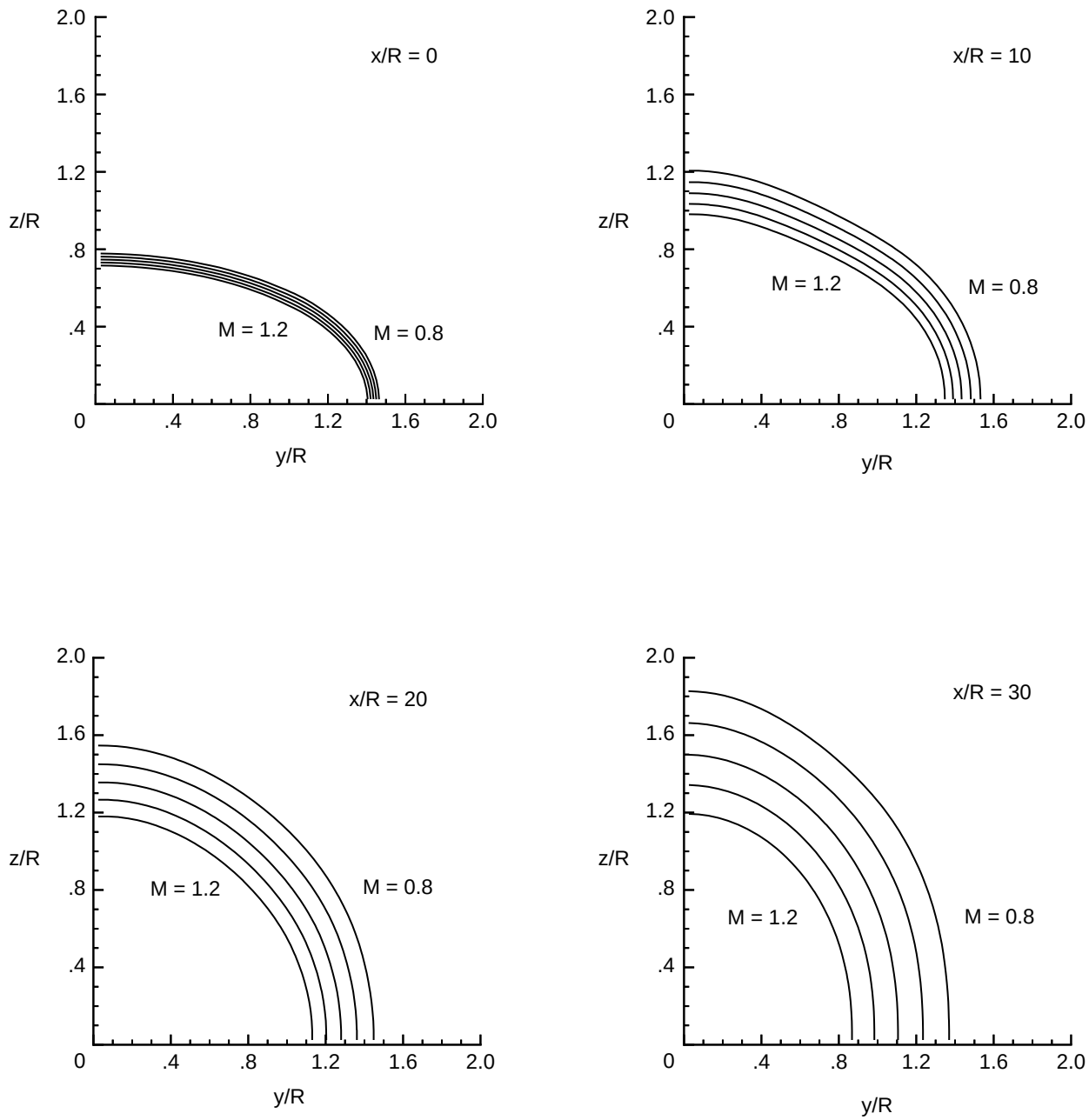

Figure 22. Cross-section shape evolution in streamwise direction of elliptic underexpanded supersonic jet. Shape aspect ratio = 2.0; Jet exit Mach number = 2.0; NPR = 11.12; p_e/p_o = 1.445.

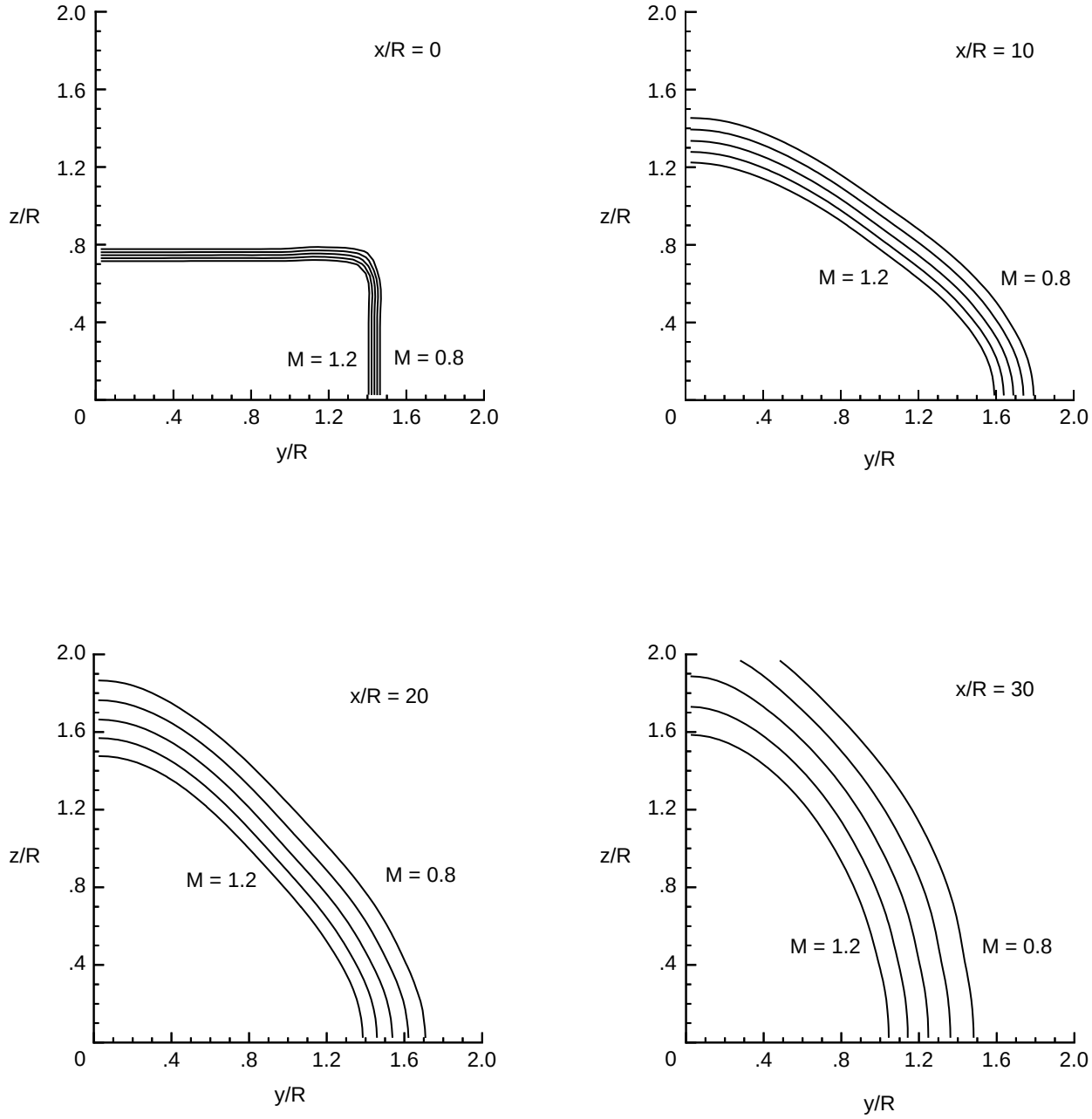

Figure 23. Cross-section shape evolution in streamwise direction of rectangular underexpanded supersonic jet. Shape aspect ratio = 2.0; Jet exit Mach number = 2.0; NPR = 11.12; p_e/p_o = 1.445.

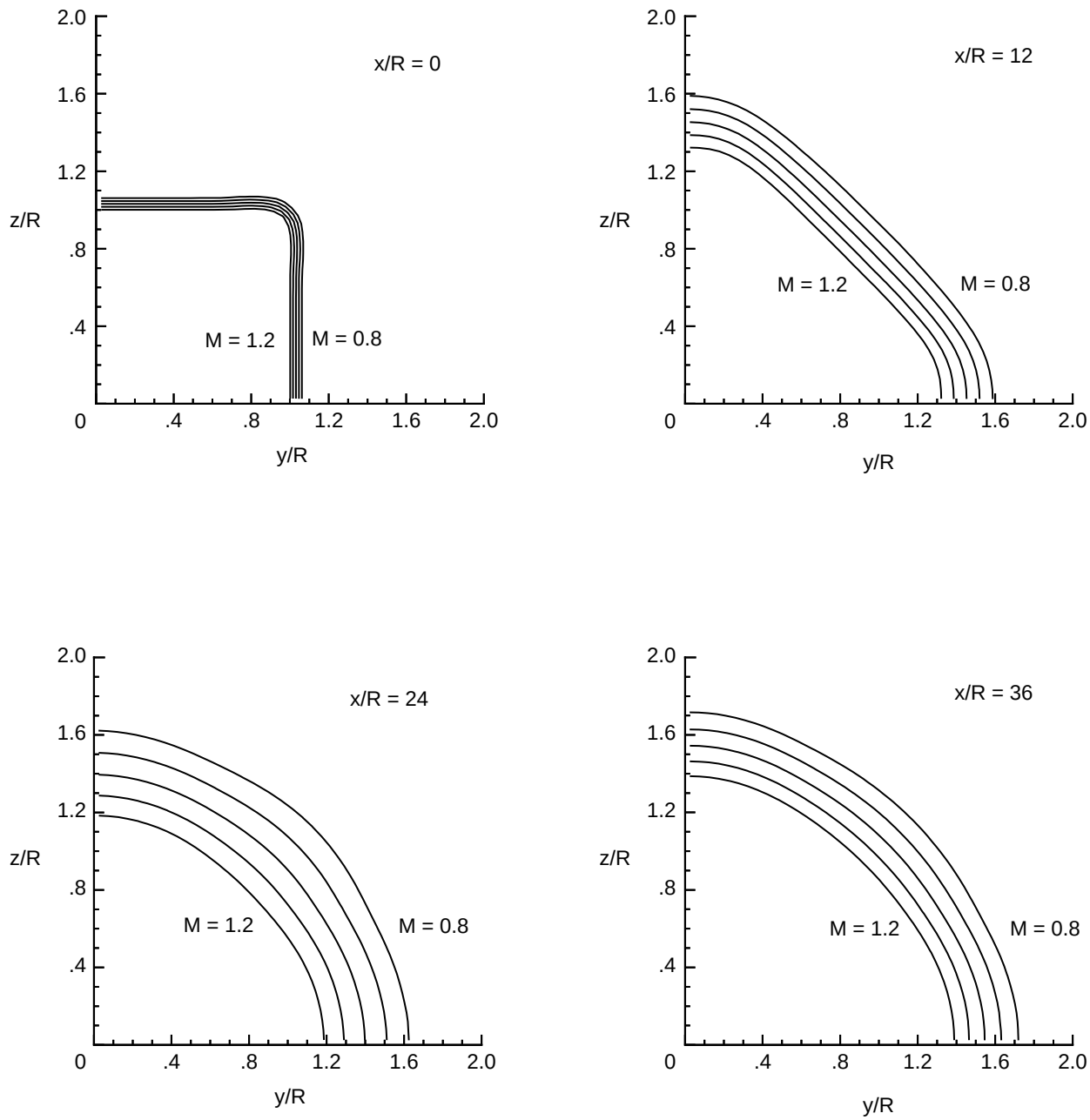

Figure 24. Cross-section shape evolution in streamwise direction of square underexpanded supersonic jet. Jet exit Mach number = 2.0; NPR = 11.12; p_e/p_o = 1.445.

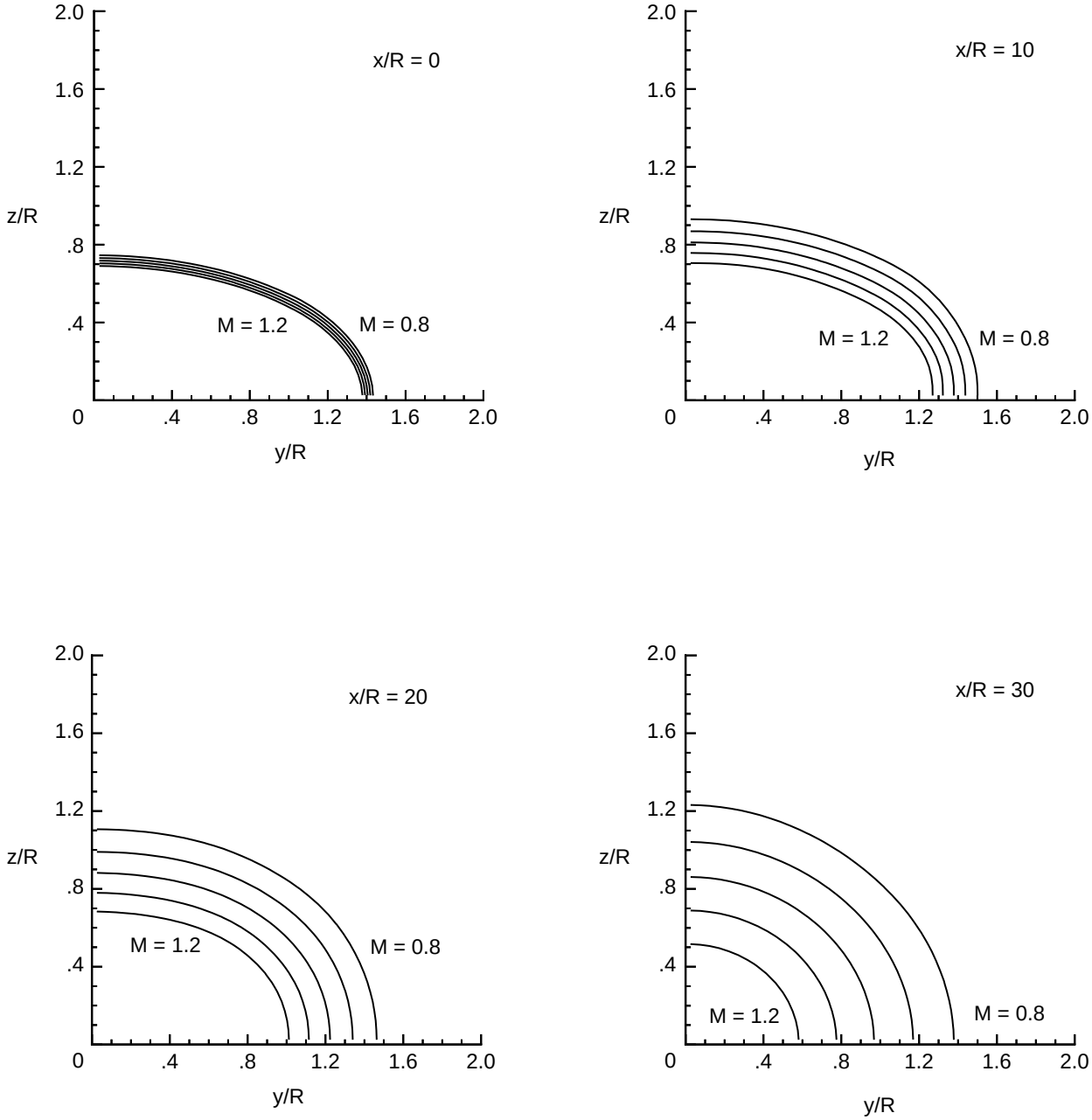

Figure 25. Cross-section shape evolution in streamwise direction of on-design elliptic supersonic jet. Shape aspect ratio = 2.0; Jet exit Mach number = 2.0; NPR = 7.82.

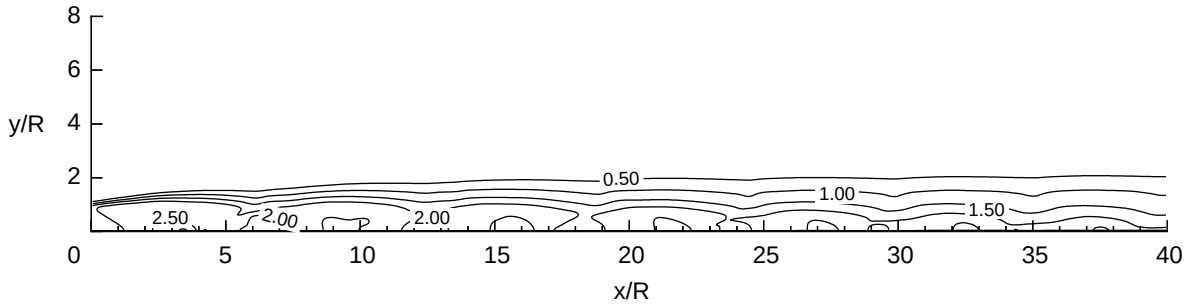

(a) Mach number contours in plane of symmetry; Interval = 0.50.

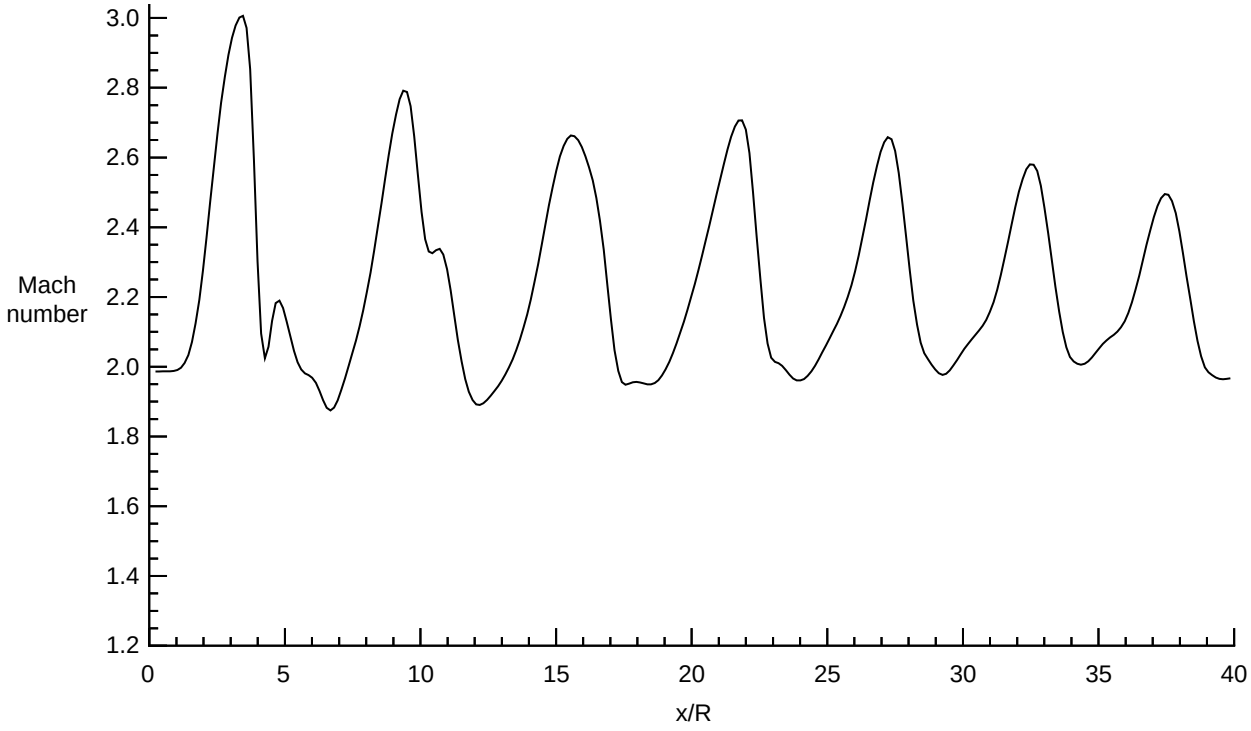

(b) Centerline Mach number profile.

Figure 26. Mach number distribution in underexpanded square jet. Exit Mach number = 2.0; NPR = 11.12.

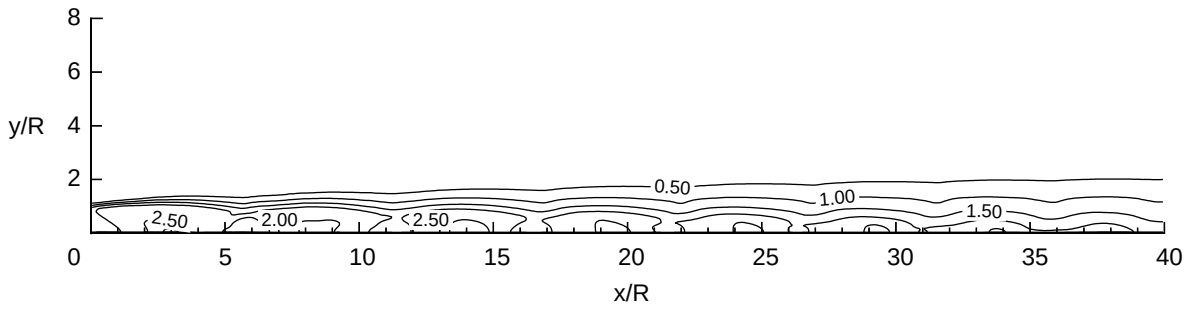

(a) Mach number contours in plane of symmetry; Interval = 0.50.

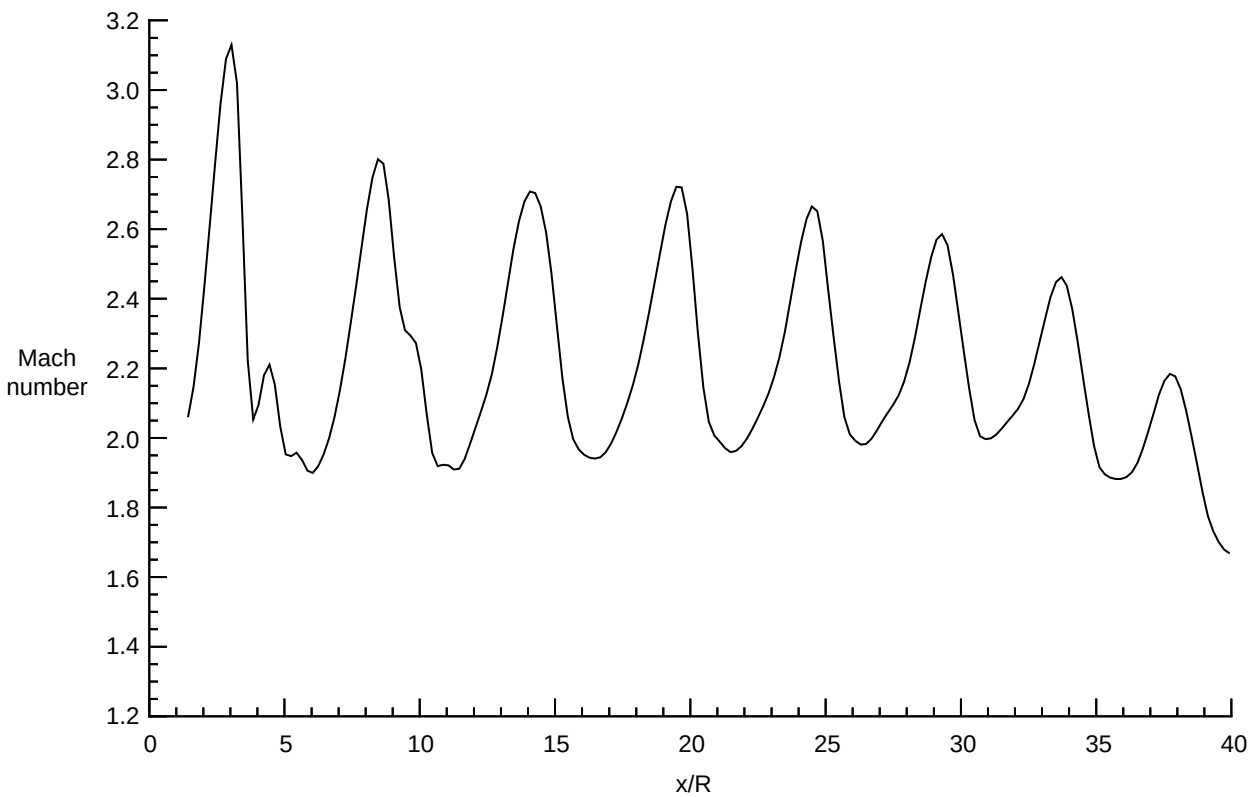

(b) Centerline Mach number distribution.

Figure 27. Mach number distribution in underexpanded circular jet. Exit Mach number = 2.0, NPR = 11.12.

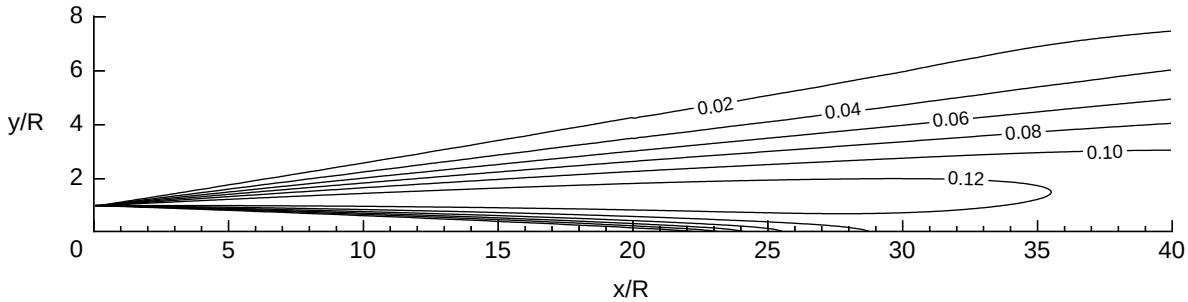

(a) Turbulence intensity distribution in plane of symmetry; u_t'/U_e contours.

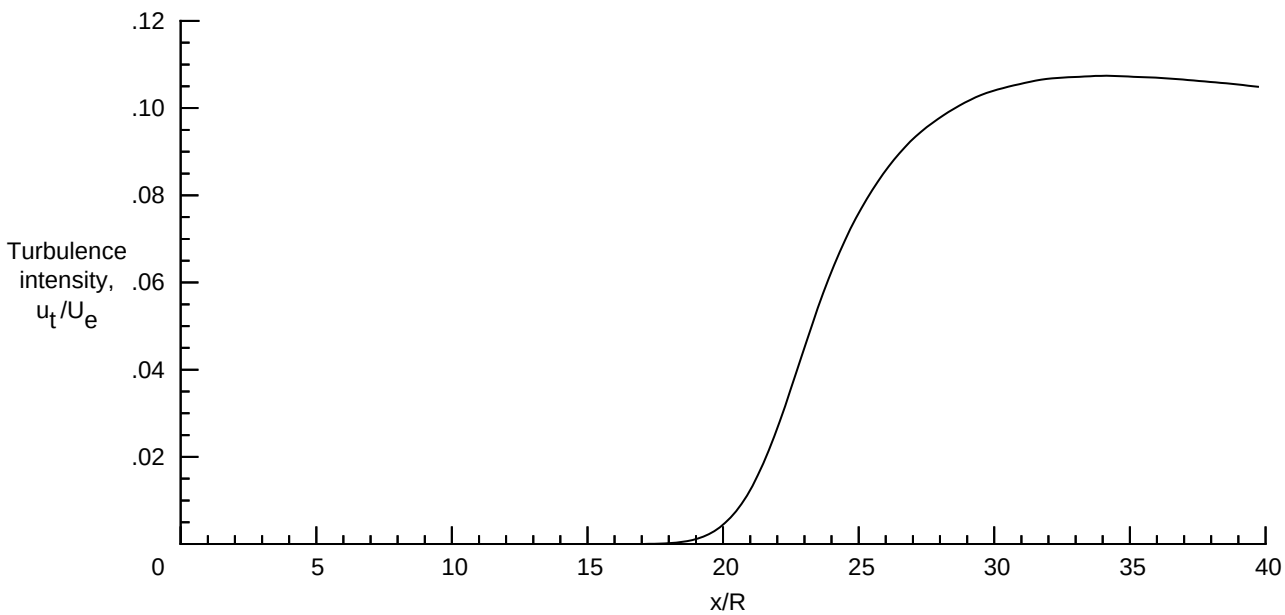

(b) Centerline turbulence intensity distribution.

Figure 28. Turbulence intensity distribution in circular jet computed by using single cell wedge grid. Exit Mach number = 2.0; on-design NPR = 7.82.

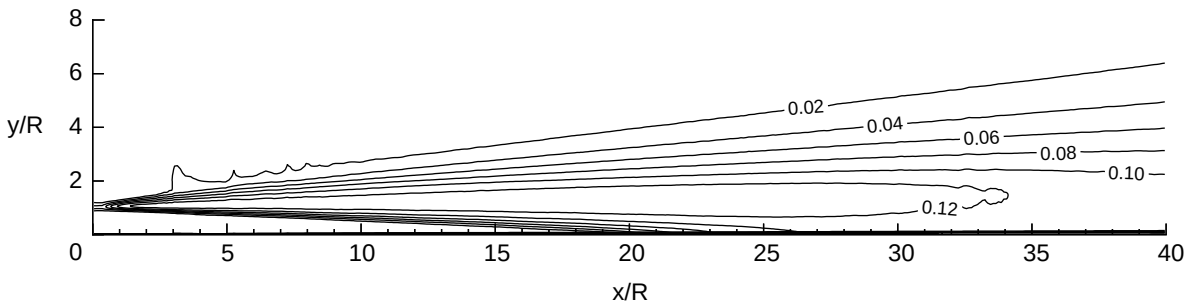

(a) Turbulence intensity distribution in plane of symmetry, u_t'/U_e contours.

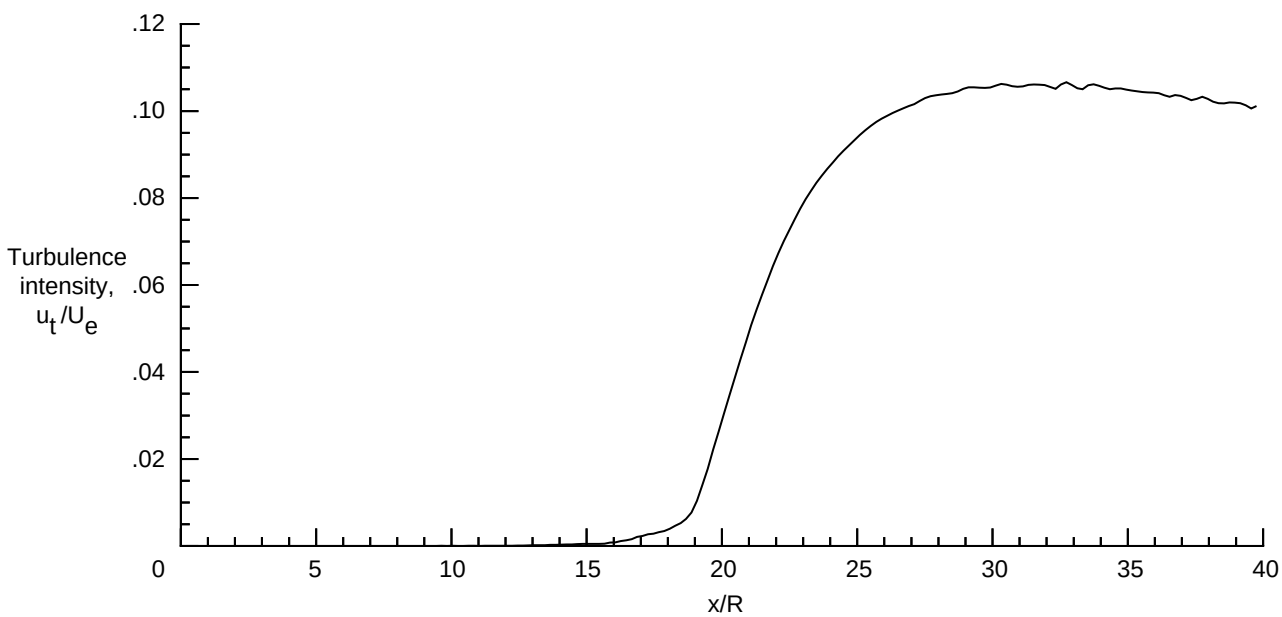

(b) Centerline turbulence intensity distribution.

Figure 29. Turbulence intensity distribution in circular jet computed by using three-dimensional adaptive grids. Exit Mach number = 2.0; on-design NPR = 7.82 ; medium grid density: *j*, *k* = 40.

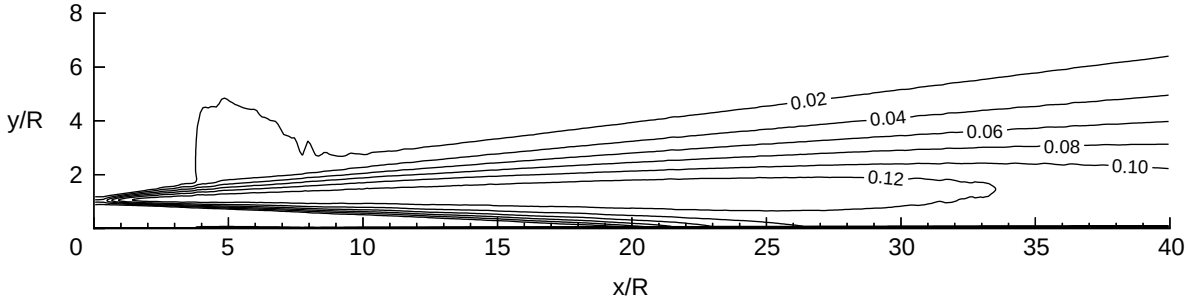

(a) Turbulence intensity distribution in plane of symmetry, u_t'/U_e contours.

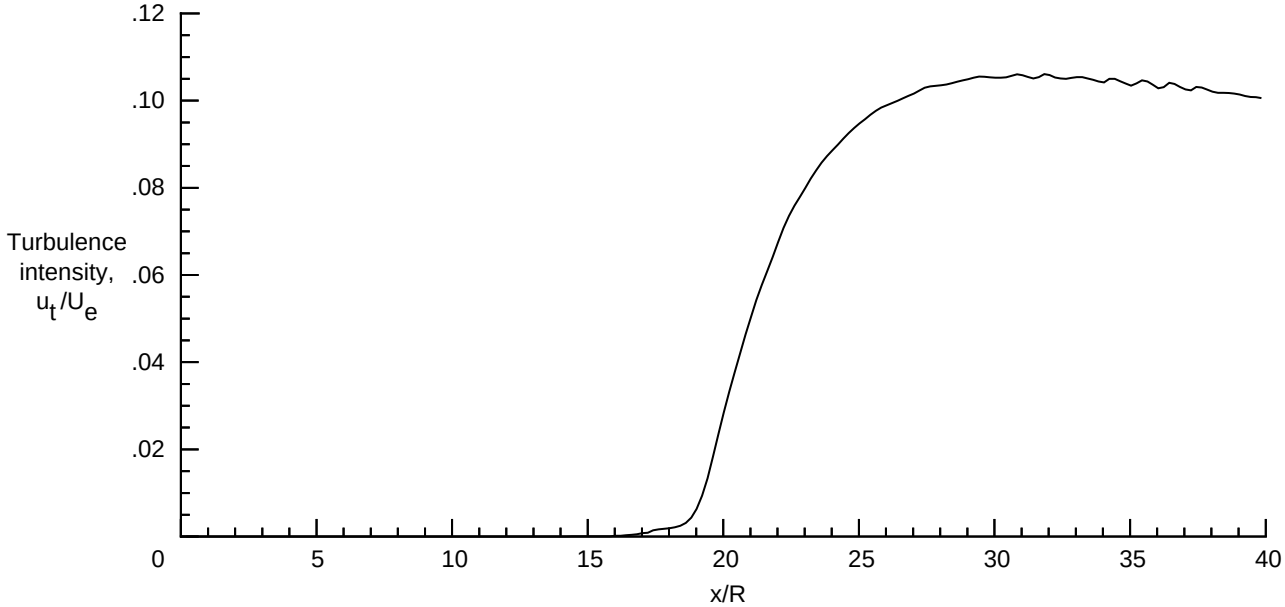

(b) Centerline turbulence intensity distribution.

Figure 30. Turbulence intensity distribution in circular jet computed by using three-dimensional adaptive grids. Exit Mach number = 2.0; NPR = 7.82; high density adaptive grid: *j*, *k* = 56.

REPORT DOCUMENTATION PAGE

Form Approved
OMB No. 0704-0188

Public reporting burden for this collection of information is estimated to average 1 hour per response, including the time for reviewing instructions, searching existing data sources, gathering and maintaining the data needed, and completing and reviewing the collection of information. Send comments regarding this burden estimate or any other aspect of this collection of information, including suggestions for reducing this burden, to Washington Headquarters Services, Directorate for Information Operations and Reports, 1215 Jefferson Davis Highway, Suite 1204, Arlington, VA 22202-4302, and to the Office of Management and Budget, Paperwork Reduction Project (0704-0188), Washington, DC 20503.

1. AGENCY USE ONLY *(Leave blank)*

2. REPORT DATE
September 1996

3. REPORT TYPE AND DATES COVERED
Technical Paper

4. TITLE AND SUBTITLE
Numerical Simulation of Jet Aerodynamics Using the Three-Dimensional Navier-Stokes Code PAB3D

5. FUNDING NUMBERS
WU 505-59-70-04

6. AUTHOR(S)
S. Paul Pao and Khaled S. Abdol-Hamid

7. PERFORMING ORGANIZATION NAME(S) AND ADDRESS(ES)
NASA Langley Research Center
Hampton, VA 23681-0001

8. PERFORMING ORGANIZATION REPORT NUMBER
L-17516

9. SPONSORING/MONITORING AGENCY NAME(S) AND ADDRESS(ES)
National Aeronautics and Space Administration
Washington, DC 20546-0001

10. SPONSORING/MONITORING AGENCY REPORT NUMBER
NASA TP-3596

11. SUPPLEMENTARY NOTES
Pao: Langley Research Center, Hampton, VA; Abdol-Hamid: Analytical Services & Materials, Inc., Hampton, VA.

12a. DISTRIBUTION/AVAILABILITY STATEMENT
Unclassified–Unlimited
Subject Category 02
Availability: NASA CASI (301) 621-0390

12b. DISTRIBUTION CODE

13. ABSTRACT *(Maximum 200 words)*
This report presents a unified method for subsonic and supersonic jet analysis using the three-dimensional Navier-Stokes code PAB3D. The Navier-Stokes code was used to obtain solutions for axisymmetric jets with on-design operating conditions at Mach numbers ranging from 0.6 to 3.0, supersonic jets containing weak shocks and Mach disks, and supersonic jets with nonaxisymmetric nozzle exit geometries. This report discusses computational methods, code implementation, computed results, and comparisons with available experimental data. Very good agreement is shown between the numerical solutions and available experimental data over a wide range of operating conditions. The Navier-Stokes method using the standard Jones-Launder two-equation k-ε turbulence model can accurately predict jet flow, and such predictions are made without any modification to the published constants for the turbulence model.

14. SUBJECT TERMS
Jet; Computation; Fluid dynamics

15. NUMBER OF PAGES
43

16. PRICE CODE
A03

17. SECURITY CLASSIFICATION OF REPORT
Unclassified

18. SECURITY CLASSIFICATION OF THIS PAGE
Unclassified

19. SECURITY CLASSIFICATION OF ABSTRACT
Unclassified

20. LIMITATION OF ABSTRACT